NASA TECHNICAL MEMORANDUM

NASA TM X-62,153

NASA TM X-62,153

THE INDUCED MAGNETIC FIELD OF THE MOON: CONDUCTIVITY PROFILES AND INFERRED TEMPERATURE

C. P. Sonett, B. F. Smith, D. S. Colburn, G. Schubert, and K. Schwartz

Ames Research Center
Moffett Field, Calif. 94035

University of California
Los Angeles, Calif. 90024

and

American Nucleonics Corporation
Woodland Hills, Calif. 91364

May 1972

The Induced Magnetic Field of the Moon:

Conductivity Profiles and Inferred Temperature

C. P. Sonett, B. F. Smith, D. S. Colburn
NASA Ames Research Center
Moffett Field, California 94035

G. Schubert
Dept. Planetary and Space Science
University of California, Los Angeles, 90024

K. Schwartz
American Nucleonics Corporation
Woodland Hills, California 91364

ABSTRACT

Electromagnetic induction in the Moon driven by fluctuations of the interplanetary magnetic field is used to determine the lunar bulk electrical conductivity. The earlier data is now augmented by an order of magnitude. The present data clearly show the North-South and East-West transfer function difference as well as the high frequency rollover suggested earlier. The difference is shown to be compatible over the mid-frequency range (10^{-3} to 10^{-2} Hz) with a noise source associated with the compression of the local remanent field by solar wind dynamic pressure fluctuations. The rollover of the transfer functions is shown to result from higher order magnetic multipole radiation; electric multipoles appear suppressed though a vestigial TM interaction may still be present. Models for two, three and four layer; current layer, double current layer and core plus current layer moons are generated by inversion of the data using a theory which incorporates higher order multipoles. Resolution, limited by signal/noise ratio and frequency range, restricts present models to 3 or 4 layers. Core radii conductivities generally are in the range $1200 \leq R < 1300$ km and $10^{-3} \leq \sigma \leq 3\times10^{-3}$ mhos/m; and for the conducting shell (of 3 layer models) $1500 \lesssim R \lesssim 1700$ with $10^{-4} \lesssim \sigma \lesssim 7\times10^{-4}$ mhos/m with an outer layer taken as nonconducting. The conductivity model reported earlier, with a local maximum at a depth ~250 km remains a possible configuration but is not unique. Uncertainties in

the conductivity from noise effects introduce uncertainties in thermal estimates small compared to those introduced by conductivity temperature relations. Core temperature based on available olivine data is $700^{\circ}C \lesssim T \leq 1000^{\circ}C$, well below estimated convection thresholds. If early convection and outward transport of radioactives did not occur, the primordial radionuclide distribution in the Moon was either sharply stratified and concentrated near the surface, or substantially below chondritic levels. This model cannot accomodate a lunar dynamo. Even if the bulk of the Moon were formed "cold", its outer part could have been sufficiently hot (e.g. through accretional heating) to account for the near surface melting evidenced by the existence of the maria.

INTRODUCTION

This paper reports progress in the determination of the electrical conductivity profile of the lunar interior using electromagnetic induction in the Moon caused by the solar wind. Earlier reports of this work which use the data on the sunlit lunar hemisphere, have shown that a strong global response takes place (SONETT et al., 1971a, b, c). The interpretation of this response showed that the deep layers of the Moon have substantially greater electrical conductivity than the near surface region; a conductivity $\sigma \approx 10^{-3}$ mhos/m at a depth of about 800 km has been inferred together with a rapidly decreasing conductivity as the surface was approached. Also a "spike" in the conductivity was found at a depth of about 250 km with $\sigma \approx 10^{-2}$ mhos/m. Profiles of this sort place rather stringent limits upon lunar models. The relatively low conductivity at depth implies that the deep interior is well below the melting point at the present time, a view supported by the existence of mascons (MULLER and SJOGREN, 1968) and the low seismicity of the Moon (LATHAM et al., 1971). The "spike" has been criticized on the grounds of uniqueness (KUCKES, 1971); a major point of this paper is to consider this further. The alternate analysis of lunar induction, which uses the response of the Moon to interplanetary field discontinuities as observed on the lunar darkside (DYAL and

PARKIN, 1971a, b) provides a consistent picture of the deep temperature though the two analyses still differ in several important details. A later section considers possible sources of the remaining differences and how they may be resolved.

Studies of electromagnetic induction in the Earth have a long history; following Gauss SCHUSTER (1889) demonstrated that fluctuations in the geomagnetic field could be separated into fields of internal and external origin from which a profile of the interior conductivity could be found. CHAPMAN and PRICE (1930) and LAHIRI and PRICE (1939), among others, have investigated this problem in detail. In the Earth a steep rise of the conductivity with depth is found.

In the case of the Earth the field is analysed into spherical harmonic components using surface data alone. Of the two modes, transverse magnetic (TM) and transverse electric (TE), the former is usually ignored because of the insulating property of the atmosphere, though polarization currents must still flow. For the Moon the problem is posed differently because the dynamic pressure of the solar wind tends to force the induced fields back into the Moon (SONETT et al., 1971a). This effect is modelled by introducing a surface current layer on the sunward hemisphere of the Moon which is taken to more or less perfectly confine the fields (SONETT and COLBURN, 1968; JOHNSON and MIDGLEY, 1968; BLANK

and SILL, 1969; SCHUBERT and SCHWARTZ, 1969). Since the fields are compressed into the less conducting outer shell of the Moon, a strong amplification of the induction signal takes place which aids in establishing a large signal to noise ratio. As for the Earth the TM mode appears suppressed or vanishingly small, though there remains a possibility that some TM fields are contributing to the lunar response. The TM mode has not entered into any calculations designed to invert the lunar response function into a conductivity profile (SONETT et al., 1971b, c).

Induction in the Moon has a formal similarity to scattering of radiation from a radially inhomogeneous sphere. Because of the effects of the solar wind, the scattering takes place in a supermagnetosonic stream which compounds the theoretical difficulties significantly. The results reported here assume complete confinement of the induced fields in the Moon, even on the dark side. This is an inexact representation of the problem since confinement on the dark side is incomplete. The errors introduced by the assumption of symmetry are not thought to be crucial (BLANK and SILL, 1969).

For the Earth the spectrum is available over a range of some 9 decades, whereas we are presently limited by various data gap generating features of the spacecraft systems and orbits to only about 2 decades. In spite of this

limitation, we can place important restrictions upon acceptable lunar conductivity profiles. The small frequency interval together with certain noise generating phenomena which appear on the sunward hemisphere in the Apollo 12 data create a further restriction upon the signal to noise ratio. Darkside data is presumably free of this source of interference, but other factors can contaminate that data and influence its interpretation. These include noise from the diamagnetic rarefaction wave, the possibility of contamination from volume currents in the cavity and currents on the boundaries as well as the time dependent sweeping back of lines of force into the cavity. In addition errors exist in the application of present theory based on a symmetric vacuum response, which ignores the solar wind confinement.

The present work treats a significantly larger set of time series than previously available, consisting of more than 120 hours of data. Some swaths have a time duration of 10 hours extending the low frequency limit downwards to $f = 5 \times 10^{-4}$ Hz. Although the earlier work suggested a "spike" at a radius of 1500 km, this conductivity function should be recognized as only one member of a larger set of possible profiles. We shall give quantitative fits to within one SDM (standard deviation of the means) for two layer (2L), three layer (3L), four layer (4L), current layer (CL) dual current layer (DCL) and core plus current layer (CCL)

models. A choice between these models would be aided by more data and possibly by improvement in identification of effects seated in the solar wind. However, it is important to recognize that the different models discussed in this paper share certain properties which characterize the lunar conductivity at depth in an average sense.

We shall show that the frequencies associated with the dominant response of the Moon cover the interval where higher order multipoles become significant (SCHUBERT and SCHWARTZ, 1972). The inclusion of multipoles $1 \leq \ell \leq 5$ ($\ell = 1$ for dipole) provides a satisfactory fit of the empirical data with models at the higher frequencies. Previously the high frequency behavior of model transfer functions was inconsistent with the data. The high frequency rollover in the empirical transfer function suggested in the early data is confirmed by the increased data which reduces the error estimates. The inclusion of higher orders means that the phase velocity of the incoming wave field v_p and the central angle θ between the position vector of the Lunar Surface Magnetometer (LSM) and the wave vector $\underline{k}$ must be taken into account as variables in model fitting.

The difference between the North-South (A_z) and East-West (A_y) transfer functions in the earlier data remains. At low frequencies this difference is probably caused by the modulation of the remanent field at the Apollo 12 site by fluctuations

of the solar wind dynamic pressure. At higher frequencies the higher order multipoles, which are basically asymmetric, complicate the interpretation of the A_y , A_z difference.

EMPIRICAL TRANSFER FUNCTIONS

Figure 1 shows the amplitudes of the three transfer functions A_x , A_y , and A_z based upon data from the first three lunations of the Apollo 12 LSM and from the Ames magnetometer on the Explorer 35 lunar orbiter. The time series used in determining these transfer functions include 47 one hour swaths and 20 nonoverlapping two hour swaths from lunations 1, 2, and 3. Seven 10 hour swaths which partially overlap the above data are included to extend the frequency downwards. The definition of the coordinate system follows that used before, where positive x is in the direction of the outward pointing unit normal to the lunar surface and positive y and z are eastward and northward, respectively, at the magnetometer site (SONETT et al., 1971b, c). The transfer functions are defined by

$$A_i(f)h_{1i}(f) = h_{1i}(f) + h_{2i}(f) \qquad (1)$$

where $h_{1i}(f)$ and $h_{2i}(f)$ are the Fourier transformed time series of the free stream interplanetary magnetic field and the magnetic field induced in the Moon, respectively. The total field transform $h_{1i} + h_{2i}$ is measured by the LSM and the incident field by the Explorer 35 Ames magnetometer. The parameter f is the frequency and the subscript i is x, y, or z. To obtain these transfer functions a large number of data time

series are employed in generating an equal number of Fourier transforms. For each pair of transforms obtained from LSM and Explorer 35 we compute the amplitudes of the transfer functions. An average of these at each frequency then yields composite transfer functions of improved accuracy.

The standard deviation of the mean is determined by the spread of the values from the ensemble of individual transfer functions according to

$$SDM_i^2 = \frac{1}{n(n-1)} \sum_{k=1}^{n} \left\{ |A_i(k)| - \frac{1}{n} \sum_{j=1}^{n} |A_i(j)| \right\}^2 , \qquad (2)$$

where j and k are the indices labelling particular time swaths and n is the total number of time swaths used. SONETT et al., (1971c) showed that when the individual differences between values of A(f) and the mean were normalized at each value of f by the standard deviation, the final distribution was approximately Gaussian (normal).

The data shown in Fig. 1 correspond to the lunar response vs. frequency for the sunlit hemisphere of the Moon. The reduced scatter in the data from that reported earlier reflects the significantly increased volume of Apollo 12 data now available and the elimination of data with faulty or otherwise noisy properties. Although the Explorer 35 Nyquist frequency F_N is 0.08 Hz, the data shown are restricted to 0.04 Hz to eliminate data possibly subject to digitization noise and filter recoloring uncertainty

which are more important at high frequencies. The low frequency limit is determined by the length T of the longest records available. We use a low frequency limit of $15/T$.

As before A_x is nearly unity over the frequency interval, and the scatter is substantially reduced. This lends confidence to a model where confinement is nearly perfect. However, at intermediate and low frequencies, A_x appears to be slightly elevated over unity while at high frequency, A_x approaches 0.8. The former suggests the creation of noise (see section on Corrections for Plasma Noise) while at the high frequencies the simplest model suggests imperfect confinement, though more complex possibilities exist.

Examination of the record for A_y and A_z shows the same general features as before though with considerably less noise. The distinctive feature of the difference in these transfer functions stands out clearly at all frequencies; the rolloff in response at the high frequency end of the data suggested in our earlier reports is reproduced here with great clarity. Although $A_z > A_y$ over most of the frequency span, at f = 0.02 Hz a crossover occurs beyond which $A_y > A_z$.

Figure 1 also shows the frequency ranges identified with swaths of 1-2 and 10 hr. lengths. The low frequencies up to about f = 0.0075 Hz are determined from 10 hr. swaths while the upper frequency range uses the 1 and 2 hr. lengths, with a mid-frequency range where both are used. In this range data

taken from the 1-2 hr. and 10 hr. swaths are in agreement. We attribute the high frequency rollover in the response to the effect of higher order multipoles, a belief confirmed by the crossover phenomenon and model calculations, both discussed in detail later. Some of the residual noise we believe due to plasma sources associated with the permanent field at the Apollo 12 site.

Since at the lowest frequency, A_y approaches unity TM magnetic field fluctuations in the East-West direction lie below the detectability threshold. For the low frequency A_y , A_z difference to be ascribed solely to TM interaction, the TM magnetic fluctuation field must be preferentially oriented in the North-South direction. BELCHER and DAVIS (1971) have shown such a preferential orientation of the microscale wave field in the free stream solar wind. This is a necessary but not sufficient condition for explaining the A_y , A_z difference by TM interaction. It should also be noted that a measureable TM interaction requires what seems like an unacceptably high crustal bulk electrical conductivity, i.e. $\gtrsim 10^{-7}$ mhos/m for a uniform composition and reasonable thermal gradient. The next section discusses the problem of the A_y , A_z difference in connection with anisotropic plasma noise.

CORRECTIONS FOR PLASMA NOISE

In this section we present evidence which suggests that a plasma noise source associated with the modulation of the local remanent magnetic field by fluctuations in the solar wind dynamic pressure contributes to the A_y , A_z difference. The A_y, A_z difference shows that the lunar response in the tangential magnetic field components is anisotropic (at least at the Apollo 12 site) even at low frequencies where the induction theory predicts no such effect (SCHUBERT and SCHWARTZ, 1972). To understand this anisotropy the directional properties of the driving and response functions have been investigated by considering the variations of each in the plane tangential to the lunar surface. The basic coordinate system was rotated about the x axis by an angle α measured counterclockwise from the y axis (east).

The power spectral densities P in the rotated coordinate system (denoted by primes) were obtained using

$$P_{y'}(\alpha) = \frac{(P_y + P_z)}{2} + \left(\frac{P_y - P_z}{2}\right) \cos 2\alpha + Q \sin 2\alpha$$

$$= P_{z'} \quad (\alpha \pm 90^\circ) \qquad (3)$$

where Q is the real part of the cross power spectral density. The power spectral density $P_{y'}$ is a periodic function of α with period 180° .

Figure 2 shows the effect of this rotation on the power spectral densities of both the Explorer 35 and the LSM data at f = 0.005 Hz. The power spectral densities are averages over the combined data for the first three lunations comprising 67 one and two hour data swaths. The average Explorer 35 power varies sinusoidally about a steady offset showing that the incident radiation has an apparent elliptical polarization as seen by LSM. The LSM data reflects this polarization, but the maximum in the LSM power is shifted in angle with respect to that of the Explorer power. The maximum in the LSM power at this frequency is in a direction approximately along that of the local remanent field at the site, $\alpha \approx -63^\circ$. This shift in the maximum is responsible for the observed difference in the A_y and A_z transfer functions.

The transfer functions for each swath were computed at 5 degree intervals for $-90^\circ \leq \alpha \leq 90^\circ$ at all frequencies and then averaged over all swaths at each frequency. This average transfer function is also shown as curve a in Fig. 2. An alternative method of computing the average transfer function is to take the square root of the ratio of the average powers at a given angle; this is shown as curve b in Fig. 2. These two methods give essentially the same mean transfer function in this example.

If the fluctuations in the noise field are predominantly aligned in one direction, then the LSM power normal to this

direction is noise free and represents the global lunar response to induction. For both a noise field which is incoherent with the induction field and a noise field which is coherent and in phase with the induction field, the transfer function in a direction perpendicular to the noise field is a minimum. For the case in which the noise field is coherent and out of phase with the induction field, the transfer function in a direction normal to the noise field is a maximum. There is no a priori reason to expect that the solar wind dynamic pressure fluctuations (assumed to be driving the noise field) would be coherent with the forcing field for the induction which consists mainly of Alfvén waves travelling along or near the mean field direction. Note from Fig. 2 that the minimum in the transfer function occurs in a direction approximately normal to that of the remanent magnetic field.

Thus we construct a transfer function by taking the minimum at each frequency of the average transfer function computed according to the method used for curve a in Fig. 2. This function, A_{min}, is shown in Fig. 3 along with the original $A_y(\alpha=0)$. Figure 3 also shows the frequency dependence of the direction α_{min} along which $A = A_{min}$. Curve $\alpha_{min}(f)$ rises smoothly from $\alpha = -15^\circ$ at $f = 5\times10^{-4}$ Hz to a plateau in the midfrequency range where $\alpha \sim 20^\circ$-30°. Above $f = 10^{-2}$ Hz, α again rises monotonically reaching 55° at $f = 4\times10^{-2}$ Hz. The midfrequency values of α_{min} agree with the idea that the noise source is aligned with the permanent magnetic field.

The monotonic increase in α_{min} for $f \gtrsim 10^{-2}$ Hz can be attributed to the effects of high frequency induction. At high frequencies the amplification of tangential magnetic fields is anisotropic (see next section) and can produce a shift in the direction of minimum power in the response field relative to the incident field. This phenomenon is illustrated by the following computation. Consider a spectrum of circularly polarized incident waves at several different frequencies. The power in the incident wave as it appears in the plane tangent to the Moon's surface at LSM is shown in Fig. 4 as a function of α . LSM is assumed to be at an angle $\theta = 130^{\circ}$ from the incident wave vector direction. The power in the tangential components of the total field at LSM is also shown as a function of α . The induced field was computed for a model Moon which typifies the models obtained from our inversions. At low frequency the LSM power is a simple multiple of the incident power. As f increases the position of the minimum in LSM power increases to larger values of α . From the curves of LSM and incident power, the transfer function can be calculated for any value of α . The results are also shown in Fig. 4. For f = 0.01 Hz the transfer function is almost independent of angle even though both the incident and LSM power depend strongly on α . As the frequency increases there is an increasing shift toward higher α in the minimum of the transfer function. At f = 0.04 Hz the minimum in the

transfer function occurs at $\alpha \approx 50^{\circ}$.

The behavior of α_{min} at the lowest frequencies suggests that there is some contribution, in addition to TE induction and the compressive noise source previously discussed, to the magnetic field fluctuations in the North-South direction. This contribution might be associated with TM induction (see the preceding section), however, this suggestion is a tentative one which requires further investigation.

The preference for a preferred alignment of the noise source along the permanent magnetic field direction is further illustrated by the distribution of angles at which individual transfer functions are minimized, as shown in Fig. 5 for $f = 0.01$ Hz and $f = 0.04$ Hz. At $f = 0.01$ Hz there is one peak in the distribution at an angle of about 25° which typifies other low frequency distributions. This is consistent with an interpretation based on a noise source due to an incoherent compressive effect on the steady field caused by fluctuations in the dynamic pressure of the solar wind. At $f = 0.04$ Hz the distribution displays two peaks which suggests that the compressive effect is augmented by another significant source at about 50°

The second peak at $\alpha = 50^{\circ}$ follows the anisotropic behavior of lunar induction at high frequency which rotates the direction of minimum response as discussed previously. A noise source associated with solar wind

modulation of the global induction seems unlikely because the peak power in the solar wind driving field is in the North-South direction, $\alpha = \pm 90^{\circ}$.

The evidence presented in this section for the existence of a noise source associated with the modulation of the permanent magnetic field by solar wind dynamic pressure fluctuations is further substantiated by several independent investigations. NEUGEBAUER et al. (1972) have shown evidence that the solar wind ion component is decelerated near the lunar surface, by roughly 50 km/sec. It is difficult to explain this deceleration by means other than the interaction of the solar wind plasma with the steady magnetic field at the site. Also DYAL et al. (1972) have shown that the dynamic pressure of the solar wind and the surface magnetic field intensity are related. This result was obtained by considering hourly averages ($f \cong 3 \times 10^{-4}$ Hz) so that the effects of internal induction were assumed to be small.

THE THEORETICAL LUNAR TRANSFER FUNCTION

A theory for obtaining lunar magnetic field transfer functions for arbitrary Moon models is a prerequisite to inverting the experimental data presented in the previous sections. SCHUBERT and SCHWARTZ (1972) have shown that there are two distinct transfer functions corresponding to the two orthogonal components of the tangential surface magnetic field. Their formulae are

$$\begin{Bmatrix} A_\theta \\ A_\varphi \end{Bmatrix} = \left| \sum_{\ell=1}^{\infty} \beta_\ell \frac{\lambda}{2\pi i} j_\ell \left(\frac{2\pi a}{\lambda}\right)\left(\frac{dG_\ell}{dr}\right)_{r=a} \begin{Bmatrix} \dfrac{dP_\ell^1(\cos\theta)}{\cos\theta\, d\theta} \\ \dfrac{P_\ell^1(\cos\theta)}{\sin\theta} \end{Bmatrix} \right| , \tag{4}$$

where j_ℓ are the spherical Bessel functions,

$$\beta_\ell = \frac{i^\ell (2\ell+1)}{\ell(\ell+1)} \quad , \tag{5}$$

$P_\ell^1(\cos\theta)$ are the Legendre functions, $G_\ell(r)$ are determined from the radial differential equations

$$\frac{d^2 G_\ell}{dr^2} + \left\{k^2 - \frac{\ell(\ell+1)}{r^2}\right\} G_\ell(r) = 0 \quad , \tag{6}$$

with

$$k^2 = \omega^2 \mu\varepsilon + i\omega\mu\sigma \quad , \quad \omega = 2\pi f \quad , \quad \lambda = \frac{f}{v_p} \quad , \tag{7}$$

and G_ℓ (r = 0) finite, G_ℓ (r = a) = 1. The parameters μ and ϵ are the magnetic permeability and electric permittivity respectively and σ , the electrical conductivity, is an arbitrary function of radius. In the present work we assume free space values for μ and ϵ and MKS units are used. The geometry is shown in Fig. 6. A spherical coordinate system with the polar axis in the direction of the incident wave vector and origin at the Moon's center has been employed.

Because of the difference in the θ dependence, A_θ and A_φ exhibit marked differences in their behavior as a function of the colatitude angle θ . This is shown in the upper part of Fig. 7 where the results for transfer function vs. frequency are presented for a three layer moon model for different values of θ but for a fixed value of the wave velocity. From equation (4) we can easily show that $A_\theta = A_\varphi$ at $\theta = 180^\circ$. Numerical calculations show that A_φ changes only slightly as θ is varied. As one can see in Fig. 7 , A_θ changes markedly as θ goes from 180° to 120° for those frequencies where $2\pi a/\lambda \gtrsim 1$. For low frequencies, only the dipole ($\ell = 1$) term makes any significant contribution to the transfer function which is then independent of θ .

For a given frequency, the velocity determines how many multipoles are required in the sum in equation 4. This is strongly evidenced in the second half of Fig. 7 where θ is held fixed but the velocity is varied. As the velocity is

decreased the turnover frequency in the transfer function also decreases. For a given lunar model, both the maximum in the transfer function and the frequency at which it occurs decreases with decreasing wave propagation velocity. In the calculations of this paper up to 5 multipoles are used for the higher frequencies. The use of the transfer function formulas of equation 4 overcomes the difficulties found in our earlier work where we were unable to match theoretically the slope and roll-off of the experimental transfer functions at high frequencies.

INVERSION OF THE TRANSFER FUNCTION INTO CONDUCTIVITY PROFILES

In our earlier work numerical integration of the radial induction equation for the TE mode was used to generate theoretical transfer functions for a given conductivity profile. An iterative procedure (Newton-Raphson) adjusted the conductivity model to provide a best fit of the theoretical to the empirical transfer functions. The calculation used a modal transfer function which is independent of θ but has the disadvantage that the forcing function cannot be experimentally resolved into modes. Here the higher order multipoles, up to and including $\ell=5$, are included in the inversions which are based on equation (4). It can be seen from equation (4) that the inversion requires specification of the parameters v_p and θ . The data being inverted are averages over a spectrum of these parameters, the detailed nature of which is not presently known. In lieu of a superposition of single plane wave induction solutions over this spectrum we are limited to carrying out inversions using plane waves characterized by one set of values of v_p and θ . We have investigated a range of velocities and directions to determine the sensitivity of the inversions to these parameters. Further, we have used A_θ in the inversions for the following reasons. First, the function A_φ is insensitive to θ variation, so to explore the sensitivity of the inversions to θ variations, A_θ is preferable.

Second, over most of the frequency range, the direction corresponding to A_{min} is close to East-West. Since the wave vectors lie on the average in the ecliptic plane A_θ is in fact the East-West transfer function.

In an attempt to minimize the possible contamination due to noise, the data fitted in the inversions is the A_{min} previously described. We will also present results obtained by fitting A_y to demonstrate the relative unimportance of the noise to the resultant models.

The models considered are 2, 3, and 4 layer (2,3,4L) single and double current layers (CL and DCL) and core plus current layer (CCL) . The parameters in each of these cases have been determined by iteration to minimize the difference between the amplitudes of the theoretical and the empirical transfer functions in the least squares sense. The calculation is carried out for 63 frequencies in the range $5\text{x}10^{-4} < f < 4\text{x}10^{-2}$ Hz. In the 2, 3, and 4 layer models the outer shell is assumed non-conducting, and the iterative process yields the conductivities and radii for the inner layer(s). Thus for each conducting layer, two parameters, σ_i , the conductivity, and R_i , the outer radius are determined.

Current layers are characterized by their radial position and $\sigma\delta$, the product of conductivity and thickness, δ . The current layer concept assumes $\sigma \to \infty$ as $\delta \to 0$, while maintaining $\sigma\delta$ invariant. In the pure current layer models the conductivity

outside the current layers is assumed zero. Both a double current layer model and a core plus current layer model are specified by four iteratively determined parameters. All of the above models are calculated for a number of choices of v_p and θ .

In the present work the measure of goodness of fit is defined by ϵ^2 , the sum of the squares of the differences between the calculated and the empirical values of A(f).

Figure 8 shows a representation of the different model conductivities computed for v_p = 200 km/sec and θ = 150° in a fit to A_{min}. The values of ϵ^2 are to be compared with the sum of the squares of the SDM's for all the 63 frequencies (0.65 for A_{min}). The hyperbolae associated with the current layers are the loci of $\sigma\delta$ = constant centered at the calculated R values. However, it should be noted that as δ increases beyond about 20 km both the location of the current layer and the $\sigma\delta$ product will change significantly.

The dual current layer model (DCL) is shown with the outer current layer having electrical admittance 59 mhos and the inner current layer 424 mhos. The admittance of the outer current layer in the CCL model is 46 mhos and that of the CL model is 100 mhos. The admittances and positions of the outer current layers in the DCL and CCL models are similar. The cores of the 3L, 4L and CCL models have essentially the same conductivities and nearly the same size. The 3L model

improves upon the 2L one by the addition of a core while retaining an outer conducting layer having nearly the same radius and conductivity as that of the 2L model. There is a negligible change in the fit and in the character of the conductivity profile between the 4L and 3L models.

The theoretical transfer functions corresponding to the models of Fig. 8 are shown in Fig. 9 together with the empirical data for A_{min}. The transfer functions of the 2L and CL models are poor fits to the data particularly at the low frequencies, emphasizing the importance of the inner core in the 3L, 4L, and CCL models. The locations of the current layers in the DCL model are consistent with the 3L model according to the following argument. The transfer fuction for a DCL model is expected to be only moderately changed as the layer thicknesses increase. Following the hyperbolae to a model in which the conductivities of the two current layers match those of the two conducting layers of the 3L model, it is seen that the outer edges of the current layers coincide with the corners of the 3L model profile. In both models damping tends to occur at two regions in the lunar interior, at approximately R = 1600 km for the higher frequencies and R = 1300 km for the lower frequencies.

The dependence of 3L models on the parameter θ is illustrated in Fig. 10 for v_p = 200 km/sec. From the ϵ^2

values it is clear that the best fits are obtained for $\theta = 150^\circ$ and 180° . This can also be seen by comparing the theoretical transfer functions of the models to the empirical data A_{min} (also shown in Fig. 10). For the larger angles the radii of the conducting layers decrease and their conductivities increase with decreasing θ . At $\theta = 120^\circ$ the iteration routine converged to nearly a CL model. As judged by ϵ^2 the fit was relatively poor.

The way in which the 3L models depend on v_p is shown in Fig. 11 for $\theta = 150^\circ$. The outer layer radius decreases and its conductivity increases with increasing v_p. The behavior of the inner layer is less predictable. Best fits are obtained for phase velocities of 200 or 300 km/sec. The preference of these better fits for the smaller phase velocities (compared to the solar wind speed of about 400 km/sec) suggests that wave normals oblique to the solar wind are present, since the phase velocity of incident waves is the sum of the solar wind speed resolved along $\underline{k}$ and the wave velocity in a reference frame comoving with the plasma.

The parameters of all our best fit models to the data A_{min} are summarized in Tables 1 - 5. The 3L and 4L monotonic models for which $\epsilon^2 \lesssim 0.7$ have outer conducting layers whose conductivities lie between about 1.1 and 6.6×10^{-4} mhos/m and whose outer radii lie between about 1500 and 1710 km.

Even the two layer models wherein $\epsilon^2 \lesssim 1$, though they are poor fits to the low frequency data, have conductivities and radii which fall within these ranges. The cores of the 3L and 4L models have conductivities varying between 1.3 and 2.2×10^{-3} mhos/m and radii varying between 1170 and 1330 km. The cores of the CCL models for which $\epsilon^2 \lesssim 0.7$ vary in conductivity between 1.2 and 2.4×10^{-3} mhos/m and vary in radius between 1210 and 1360 km. Although no unique model can be inferred from inversion of the data, the 3L and 4L monotonic models are all in substantial agreement and characterize the average properties of monotonic conductivity profiles. The cores of the 3L, 4L and C+CL models are in particularly close agreement among themselves. Since the electrical conductivity of geologic material is an exponential function of the inverse temperature, the differences in conductivity among the various 3L and 4L models are relatively unimportant in assessing the lunar temperature at depth.

Certain 4L fits resemble more closely the CCL model rather than a monotonic fit. For example, at v_p = 400 km/sec, $\theta = 180^\circ$, the outer layer is 14 km thick centered around R = 1472 km with a conductivity giving $\sigma\delta$ = 34 mhos. This is separated from the core by a region of low conductivity. The CCL model gives $\sigma\delta$ = 84 mhos at R = 1467 km with a comparable core. Similarly at v_p = 300 km/sec, $\theta = 150^\circ$, the relatively highly conducting outermost layer can be

described by R = 1474 km, $\sigma\delta$ = 68 mhos. The CCL model has R = 1476 km, $\sigma\delta$ = 78 mhos, the cores again being similar. The inclusion of a conductivity peak superimposed on a monotonic profile as proposed earlier is seen by the low ϵ^2 values of the CCL fits to be among the possible fits to the present data.

The CCL and DCL models for which $\epsilon^2 \lesssim 0.7$ have outer current layers whose $\sigma\delta$ products vary between about 32 and 115 mhos and whose radii vary between about 1440 and 1590 km. The poorer fitting CL models also tend to group in this region. As was the case with the monotonic models, the models with current layers are in substantial agreement among themselves. Furthermore, as the thickness of current layers is allowed to increase, the models yield conductivities in agreement with those of the 3L and 4L monotonic models.

A scanning of the ϵ^2 values shows a preference for certain velocity and angle ranges. The best fits are obtained for θ = 180° or 150°, with the fits becoming substantially poorer for θ = 120°. The ϵ^2 values for v_p = 200 or 300 km/sec are generally smaller than those for v_p = 400 km/sec, although acceptable fits are found for v_p = 400 km/sec.

Generally it appears that the electromagnetic transfer function is reasonably sensitive to changes in the conductivity model, but differences in the determination of the lunar temperature will be attributed more to lack of knowledge of

the proper conductivity-temperature function than to differences in the different conductivity profiles.

In Tables 6-10 we present the results of the different model fits to the A_y data, for which $\epsilon^2 = 1.1$. For the most part the models which best fit the A_y data have parameter values which lie within the ranges of variability defined by the model fits to A_{min}.

DISCUSSION OF CONDUCTIVITY MODELS

The model inversions have been based upon two versions of the transfer function. Also two new variables, θ , and v_p have been introduced to account for the more complex geometry encountered when the higher order multipoles are included and the inversions have been carried out using A_θ . The possibility that A_φ is sometimes important must be considered. Although A_θ is a strong function of θ , A_φ varies only slowly, and for all values of θ investigated here $A_\theta \geq A_\varphi$, the equality holding at $\theta = 180^\circ$. Using the model of the calculation whose results are shown in Fig. 4, the value of A_φ changes from 2.1 to 2.3 when θ is changed from 180° to 130° at f = 0.04 Hz. Thus A_φ ($\theta = 180^\circ$) is a reasonable approximation to A_φ over a wide range of θ . For cases where $\underline{k}$ is out of the ecliptic, a mixture of A_θ , A_φ responses is expected. This will modify the net response somewhat, decreasing the sensitivity of the transfer function to changes in θ . A similar effect is expected when a superposition over a spectrum of plane waves is used in determining transfer functions. Thus the values for θ and v_p are tentative and subject to improvement.

We have shown a wide range of model conductivities based upon both A_y (taken to be identical to A_θ in the average sense) and a noise corrected version of the transfer function, A_{min}. Both may be subject to some mixing between A_θ and A_φ . These

effects cannot be important at mid and low frequencies where the induction is nearly purely dipolar. The models all show a conductivity at about R = 1200 to 1350 km in the range of about $1\text{-}2.5\text{x}10^{-3}$ mhos/m. Conductivity below about 1100 km radius cannot yet be measured because of the strong damping of the low frequencies at that level. An extension to lower frequency and possibly improvement in the signal to noise ratio will be required. The alternate model of a current layer at that depth as part of the DCL model also cannot be ruled out and would likely be due to material of anomalous conductivity at that depth; there appears no reason to pursue this line of reasoning at the present time.

The close fit of the DCL and CCL models show that the high frequency behavior can also be modeled by a near surface equivalent current layer. Although there is a basis in lunar evolutionary theories for introducing a model with a conductivity "spike" at about R = 1500 km, and the earlier calculations yielded such a model, it is only one of a class of possible models. Although the low frequency behavior is relatively independent of details of the solar wind geometry, the latter has an important influence upon the radius of the outer shell and less so upon the average conductivity of the shell. An extension of our model calculations to include the superposition of plane waves is required before accurate values for the conductivity and radius of the

outer conducting shell are determined. The model fits indicate that these parameters vary between about $1\text{-}6\times10^{-4}$ mhos/m and 1500-1700 km. None of the variations discussed are large and therefore the existence of a noise field of the magnitude suggested by the rotation investigation does not pose a fundamental difficulty at the level of resolution available.

The lunar conductivity profiles which are based upon darkside data (DYAL and PARKIN, 1971a, b) differ somewhat from the ones presented here, but the temperatures which the models imply are never different by more than about 200°C. The deep conductivity reported by DYAL and PARKIN (1971a,b) is $\approx 10^{-2}$ mhos/m based upon 5 observations of the extended "tail" of the transient response. It is not possible to reconstruct their argument completely but the principal issue is that the response is thought to last in excess of 15 minutes. If their detectability implies that the transient decays to 15% of the final value, this equals two e-fold times; if 5% three e-folds. Thus the "time constant" is 450 seconds for the first case and 300 seconds for the second. "Time constants" determined from the models of this paper lie in the range of about 300 sec to 200 sec; thus if the Dyal-Parkin 15 minutes represents a detection limit, the value is in accord with our "time constant" and their internal conductivity should be altered downwards. However, it is difficult to determine their time bound since at least in one case it is stated to

last longer than 15 minutes. An additional potential complication arises from the possibility of contamination of the transient response by a time variable forcing function. Inspection of their Fig. 13 (DYAL and PARKIN, 1971a) shows a large scatter of cases for transients lasting longer than 4 minutes; indeed anywhere from 28-38% of the cases examined in x, y, or z show evidence for complete relaxation by 4 minutes suggesting the possibility of a nonsteady forcing function.

A similar problem associated with the assumption of step forcing functions has been discussed by SCHUBERT and COLBURN (1971). In this case account needs to be taken of the finite time for the whole Moon to become immersed in a convected field change, requiring as a first approximation a ramp input for the forcing function. Errors in the interpretation of the high frequency response are connected with this effect and have an important influence upon the final values found for the shell radius and conductivity.

Although an accurate high frequency comparison of the darkside and sunlit side data cannot yet be made because of complications with the solar wind geometry, it is instructive to show a forward calculation for the comparative models. In Fig. 12 we show the three layer best fit models for both A_y and A_{min} compared to a similar calculation for the Dyal-Parkin three layer models using the same solar wind parameters, i.e. v_p = 200 km/sec and $\theta = 150^\circ$. The curves labelled DP_1 and DP_2 respectively are based on the models of DYAL and

PARKIN (1971a, b) and DYAL and PARKIN (private communication). The departures at low frequency are associated with the core (their core is more highly conducting but deeper) while at high frequencies the DP_2 model fits the A_y data quite well. The DP_1 model is a poor fit everywhere to both the A_{min} and A_y transfer functions. It is worth noting that an incoherent noise source for the sunlit side models should mean that A_{min} is a more realistic transfer function; however, the DP_2 model does not fit A_{min}. Clearly further work is required on both approaches in order to effect a reconciliation between the results.

LUNAR TEMPERATURE

Transformation of the conductivity profile into a thermal profile rests upon use of conductivity-temperature functions which are poorly known. Also some assumption must be made regarding the composition of the interior at the relevant depths. The more resistive the matter the higher will be the estimate of the temperature. Following our earlier estimate we use olivine as the material. Much laboratory work has been carried out on this substance though the values for activation energy, E , and mobility, σ_0 , vary widely. The early values determined by HUGHES (1955) yield conductivities generally lower than later determinations, but all values are somewhat suspect. ENGLAND et al. (1968) show a conductivity function which is widely quoted; it uses an electronic term from HUGHES (1955) and an ionic term from BRADLEY et al. (1964). Thus this is a composite once removed from direct determination. However, the activation energies in the various determinations are not too far apart, and the greatest variation is in the mobility where differences of an order or two can occur.

KOBAYASHI and MARUYAMA (1971) have studied single olivine crystals. The principal cause of variation in activation energy and mobility is the iron content expressed as the fayalite fraction (Fa). The variation is mostly in σ_0 with

$\sigma_0 = 8x10^{-2}$ *mhos/m for Fa = 0 (SHANKLAND, 1969) and* $\sigma_0 = 20$ mhos/m for Fa = .20. SHANKLAND (1969) found that the activation energy changed by an order of magnitude as Fe was added to pure forsterite, but this might be a saturation effect at a very small concentration of Fe, since the results of KOBAYASHI and MARUYAMA (1971) for $0.074 < Fa < 0.126$ show constant single crystal activation energies. In summary, from this work we can expect about a 2.5 order difference in σ_0 as the Fa content varies from zero up to 20 per cent. Recently HOUSLEY and MORIN (1972) have shown that spurious effects associated with thermionic emission can raise the conductivity estimates of olivine and introduce an error of several hundred degrees in temperature in the neighborhood of 1000°C.

In spite of these limitations we are substantially aided by the logarithmic dependence of temperature upon conductivity. Thus an order error means approximately a 100-200 degree error in temperature. The ENGLAND et al. (1968) formula yields a deep temperature of about 800°C and a shell temperature of about 600°C. Although the constants differ, the NORITOMI (1961) olivines yield approximately the same temperature, i.e. about 700°C. It should also be noted that the single crystal determinations of KOBAYASHI and MARUYAMA (1971) yield temperatures ranging from about 750-1000°C while the Fa mole fraction decreases from 12.6 to 7.4 per

cent. The final conclusion we arrive at is that a central temperature in the neighborhood of 800-1000°C is probable, based upon current data for olivines. More conducting matter would depress the computed temperature while an increase in resistivity at a given temperature would require an upward revision. For the outer conducting shell further work is required to refine the temperature estimate. Values cluster about our present estimate of 600° C based upon the ENGLAND et al. (1968) formula and a uniform olivine Moon.

A "cold" Moon places serious constraints upon any theory of its origin and evolution (REYNOLDS et al., 1972; HAYS, 1972; PAPANASTASSIOU et al., 1970; UREY and MACDONALD, 1971). A chondritic Moon would by today have melted unless perhaps convection would preclude it (RUNCORN, 1967; TURCOTTE et al., 1972). Other possible sources of thermal energy such as fossil nuclides (FISH et al., 1960), accretional energy (WOOD, 1972; HANKS and ANDERSON, 1969; SONETT and COLBURN, 1970), electrical heating during formation (SONETT et al., 1970), tidal friction during a hypothetical capture (KAULA, 1966), and lastly a "hot" start by formation within a dusty neighborhood at an elevated temperature would require the long lived radionuclide budget to be reduced in order to meet the boundary condition of a low central temperature.

A potentially serious additional constraint upon the thermal history is the presence of ubiquitous magnetism in lunar rocks.

Possible origins for the magnetism have been discussed elsewhere (SONETT and RUNCORN, 1971). The simplest source for the background field required for rock magnetization lies in a lunar dynamo. The dynamo would have had to operate as early as 0.6 aeons after formation implying a molten convecting core (presumably iron) at that time. This would be difficult to achieve without a "hot" start and additional heating, both being incompatible with a cold Moon unless the heat were subsequently convected out.

The comments made assume a Moon in which the radioactivity was laid down uniformly; a gross inhomogeneity in the radial concentration of nuclides could alter the picture and possibly yield a viable model, though much more complex.

CONCLUSIONS

We have shown a number of conductivity profiles for the Moon which differ at most in detail and mostly in regions near to the surface. All models yield a deep conductivity (R = 1100-1300 km) of about $1\text{-}3\times10^{-3}$ mhos/m. Conversion of this value to temperature using reasonable olivine conductivity functions yields a temperature at that depth of about 800° C which could be low by as much as 200 degrees. Thus a major conclusion of this paper which substantiates earlier reports (SONETT et al., 1971b, c; DYAL and PARKIN, 1971a, b) is that the central temperature of the Moon is well below the melting point. Large increases in temperature below the level where the deepest sounding takes place are ruled out for a Moon which is reasonably well behaved thermally because of the excessive thermal gradients required at depth.

The conclusion that the lunar interior is well below the melting point at the present time is in accord, with the low seismicity (LATHAM et al., 1970), and the existence of mascons (MULLER and SJOGREN, 1968). The recent heat flow measurement (LANGSETH, 1972) is in disagreement if this measurement is assumed to represent a global value, but that viewpoint in turn requires a global concentration of radioactives about twice chondritic, so it appears likely that local influences are important in the interpretation of the heat flow.

The presence of thin highly conducting current layers, such as are assumed in the CL, DCL, and CCL models, are consistent with certain evolutionary models of the Moon. The low surface abundance of iron has led UREY et al. (1971) to propose the existence of a sunken layer enriched in Fe. Also RAMA MURTHY et al. (1971) have suggested the formation of sub-surface Fe-FeS mixtures as a way of depleting the lunar surface Fe abundance. A nonunique test for a conducting layer, consistent with our CCL, DCL, and CL models implies a thresh-old for the layer thickness based upon pure, consolidated Fe of 10 microns. Of course, realistically an Fe layer would likely consist of an unconsolidated layer whose mean conductivity $\bar{\sigma}$ was significantly lessened. Nevertheless even a reduction of $\bar{\sigma}$ by many orders would result in an electro-magnetic response very sensitive to such a layer.

Lastly the deep temperature surmised for the Moon appears too low to permit solid state convection to operate at the present time. However it does not rule out such convection in the past. For example if the conductivity function is in error requiring an upward revision of temperature towards an extremum of $\sim 1000^{\circ}C$, it is possible that early convection was followed by conduction, the latter causing a drop of $100\text{-}200^{\circ}C$ at 0.6-0.7 Rm over, say, 2 aeons consistent with the lunar thermal "time constant". Thus an early temperature in the neighborhood

of 1200 C could have existed, consistent with current views on the low temperature limit on solid state convection. Alternatively it is entirely possible that the rheology of lunar material is sufficiently different from that of the earth that 1200°C is not an absolute lower limit for the occurrence of solid state convection.

NOTE ADDED IN REVIEW

In work so far reported, including this paper, we have dealt only with the amplitude of the transfer function. Additional information is contained in the phase of the complex transfer function but extraction of phase information is made difficult because of several effects which are believed to occur.

The Explorer 35 and Apollo 12 magnetometers are in relative motion; the effect is to introduce a Doppler shift which affects the coherence between Explorer and LSM signals. This effect is by no means trivial because of complications introduced by the nature of the solar wind itself. Tests of the data and theoretical analysis show that the relative motion introduces a randomization which can severely limit or even destroy the coherence between the signals observed by the two instruments. Changes in the properties of the solar wind between the two points of observation will also distort the coherence. For example, the solar wind can vary between conditions wherein turbulence is locally being generated or destroyed, or a steady state level of turbulence can exist. Also changes in the magnitude or direction of the bulk velocity of the solar wind will temporarily modify the Doppler shift providing an additional source of randomization.

In view of these as yet unresolved problems we have so far discussed only the transfer function amplitude, understanding that some phase information which would likely increase resolution within the Moon is thereby lost. In later work, provided that suitable information is available, we shall attempt to reconstruct the entire transfer function and thus be in a position to comment upon the effects of the introduction of phase.

REFERENCES

BELCHER J.W. and DAVIS L. (1971) Large amplitude Alfvén waves in the interplanetary medium, 2. J. Geophys. Res. 76, 3534-3563.

BLANK J., and SILL W.R. (1969) Response of the Moon to the time varying interplanetary magnetic field. J. Geophys. Res. 74, 736-743.

BRADLEY R.S., JAMIL A.K., and MUNRO D.C. (1964) The electrical conductivity of olivine at high temperatures and pressures. Geochim. et Cosmochim. Acta 28, 1669-1678.

CHAPMAN S., and PRICE A.T. (1930) The electrical and magnetic state of the interior of the earth as inferred from terrestrial magnetic variations. Proc. Royal Soc. A 229, 427-460.

DYAL P., and PARKIN C.W. (1971a) Electrical conductivity and temperature of the lunar interior from magnetic transient-response measurements. J. Geophys. Res. 76, 5947-5969.

DYAL P., and PARKIN C.W. (1971b) The Apollo 12 magnetometer experiment: internal lunar properties from transient and steady magnetic field measurements. Proc. Second Lunar Sci. Conf., Geochim. Cosmochim. Acta, Suppl 2, Vol. 3, pp. 2391-2413. MIT Press.

DYAL P., PARKIN C.W., SNYDER C.W., and CLAY D.R. (1972) Measurements of lunar magnetic field interactions with the solar wind. Submitted to Nature.

ENGLAND A.E., SIMMONS G., and STRANGWAY D. (1968) Electrical conductivity of the Moon. J. Geophys. Res. 73, 3219-3226.

FISH R.A., GOLES G.G., and ANDERS E. (1960) The record in the meteorites. III On the development of meteorites and asteroidal bodies, Ap. J. 132, 243-258.

HANKS T.C., and ANDERSON D.L. (1969) The early thermal history of the earth. Phys. Earth Planet. Int. 2, 19-29.

HAYS J.F. (1972) Radioactive heat sources in the lunar interior. Phys. Earth Plan. Int. 5, 77-84.

HOUSLEY R.M., and MORIN F.J. (1972) Electrical conductivity of olivine and the lunar temperature profile. The Moon (In press).

HUGHES H. (1955) The pressure effect on the electrical conductivity of peridot. J. Geophys. Res. 60, 187-191.

JOHNSON F.S., and MIDGLEY J.E. (1968) Notes on the lunar magnetosphere. J. Geophys. Res. 73, 1523-1532.

KAULA W.M. (1966) Thermal effects of tidal friction - In The Earth-Moon System, (editors B.G. Marsden and A.G.W. Cameron), pp. 46-52, Plenum, New York.

KOBAYASHI Y., and MARUYAMA H. (1971) Electrical conductivity of olivine single crystals at high temperature. Earth and Planet. Sci. Lett. 11, 415-419.

KUCKES A.F. (1971) Lunar electrical conductivity profile. Nature 232, 249-251.

LAHIRI N., and PRICE A.T. (1939) Electromagnetic induction in nonuniform conductors and the determination of the conductivity of the Earth from terrestrial magnetic variations. Proc. Royal Soc. A 784, 509-540.

LANGSETH M.G., Jr., CLARK S.P., Jr., CHUTE J., Jr., and KEIHM S., The Apollo 15 lunar heat flow measurement (abstract), "Revised Abstracts of the Third Lunar Science Conference," p. 475, January, 1972.

LATHAM G., EWING M., DORMAN J., PRESS F., TOKSOZ N., SUTTON G., MEISSNER R., DUENNENBIER F., NAKAMURA Y., KOVACH R., and YATES M. (1971) Moonquakes. Science 170, 620-626.

MULLER P.M., and SJOGREN W.L. (1968) Mascons: lunar mass concentrations. Science 161, 680-684.

NEUGEBAUER M., SNYDER C.W., CLAY D.R., and GOLDSTEIN B.E. (1972) Solar wind observations on the lunar surface with the Apollo 12 ALSEP. (preprint).

NORITOMI K. (1961) The electrical conductivity of rock and the determination of the electrical conductivity of the Earth's interior. J. Mining Coll., Akita Univ., Ser. A, 7 27-59.

PAPANASTASSIOU D.A., WASSERBURG G.J., and BURNETT D.S. (1970) Rb-Sr Ages of lunar rocks from the Sea of Tranquillity. Earth Planet. Sci. Lett. 8, 1-19.

RAMA MURTHY V., EVENSON N.M., and HALL H.T. (1971) Model of early lunar differentiation. Nature 234, 267-290.

REYNOLDS R.T., FRICKER P., and SUMMERS A.L. (1972) Thermal history of the Moon. In AIAA progress series, Lunar Thermal Characteristics, editor J. W. Lucas (in press).

RUNCORN S.K. (1967) Convection in the Moon and the existence of a lunar core. Proc. Roy. Soc. A 296, 270-284.

SCHUBERT G., and SCHWARTZ K. (1969) A Theory for the interpretation of lunar surface magnetometer data. The Moon 1, 106-117.

SCHUBERT G., and COLBURN D.S. (1971) Thin highly conducting layer in the Moon: consistency of transient and harmonic response. J. Geophys. Res. 76, 8174-8180.

SCHUBERT G., and SCHWARTZ K. (1972) High frequency electromagnetic response of the Moon. J. Geophys. Res. 77, 76-83.

SCHUSTER A. (1889) The diurnal variation of terrestrial magnetism. Phil. Trans. Roy.Soc. A 180, 467-512.

SHANKLAND T.J. (1969) Transport properties of olivine. In The Application of Modern Physics to the Earth and Planetary Interiors, (editor S.K. Runcorn), Wiley, London.

SONETT C.P. and COLBURN D.S. (1968) The principle of solar wind induced planetary dynamos. Phys. Earth Planet. Interiors 1, 326-346.

SONETT C.P., and COLBURN D.S. (1970) The role of accretionally and electrically inverted thermal profiles in lunar evolution. The Moon 1, 483-484.

SONETT C.P., COLBURN D.S., SCHWARTZ K., AND KEIL K. (1970) The melting of asteroidal-sized parent bodies by unipolar dynamo induction from a primordial T Tauri sun, Astrophys. and Space Sci. 7 , 446-488.

SONETT C.P., and RUNCORN S.K. (1971) How to use magnetic fields for fun and profit. Comments on Astrophysics and Space Physics 3, 149-154.

SONETT C.P., DYAL P., PARKIN C.W., COLBURN D.S., MIHALOV J.D., and SMITH B.F. (1971a) Whole body response of the Moon to electromagnetic induction by the solar wind. Science 172, 256-258.

SONETT C.P. COLBURN D.S., DYAL P., PARKIN C.W., SMITH B.F., SCHUBERT G., and SCHWARTZ K. (1971b) Lunar electrical conductivity profile. Nature 230, 359-362.

SONETT C.P., SCHUBERT G., SMITH B.F., SCHWARTZ K., and COLBURN D.S. (1971c) Lunar electrical conductivity from Apollo 12 magnetometer measurements: compositional and thermal inferences. Proc. Second Lunar Sci. Conf., Geochim. Cosmochim. Acta Suppl. 2, Vol. 3, pp. 2415-2431. MIT Press.

TURCOTTE D.L., HSUI A., and TORRANCE K.E. (1972) Thermal structure of the Moon (preprint).

UREY H.C., and MACDONALD G.J.F. (1971) Origin and history of the Moon. In Physics and Astronomy of the Moon (editor Z. Kopal). Academic Press.

UREY H.C., MARTI K., HANKINS J.W., and LIU M.K. (1971) Model history of the lunar surface. Proc. Second Lunar Science Conf., Geochim. Cosmochim. Acta. Suppl. 2, Vol. 3, 987-998. MIT Press.

WOOD J.A. (1972) History and early magmatism in the Moon. Icarus (In press).

TABLE 1

Two Layer and Current Layer Model Fits to A_{min}

		2L			CL		
v_p ($\frac{km}{sec}$)	θ (deg)	R (km)	σ ($\frac{mhos}{m}$)	ϵ^2	R (km)	$\sigma\delta$ (mhos)	ϵ^2
400	180	1520	5.45(-4)	0.78	1442	127.0	2.55
	150	1513	5.80	0.81	1438	131.3	2.43
	130	1493	6.87	0.95	1422	146.9	2.17
	120	1469	8.56	1.30	1404	169.2	2.03
300	180	1544	4.56	0.86	1459	114.0	3.05
	150	1530	5.06	0.80	1449	122.6	2.74
	130	1496	6.68	0.90	1425	143.3	2.19
	120	1456	9.59	1.47	1394	183.0	1.97
200	180	1606	3.03	1.90	1504	88.5	5.21
	150	1578	3.65	1.34	1484	99.6	4.08
	130	1509	6.00	0.74	1435	135.1	2.32
	120	1435	1.17(-3)	1.61	1376	209.9	1.74

TABLE 2

Three Layer Model Fits to A_{min}

v_p ($\frac{km}{sec}$)	θ (deg)	R_1 (km)	R_2 (km)	σ_1 ($\frac{mhos}{m}$)	σ_2 ($\frac{mhos}{m}$)	ϵ^2
400	180	1206	1527	1.90(-3)	5.13(-4)	0.47
	150	1208	1519	1.80	5.49	0.55
	130	1181	1497	1.56	6.71	0.83
	120	1201	1471	1.06	8.33	1.28
300	180	1224	1553	1.88	4.18	0.33
	150	1194	1537	2.10	4.85	0.40
	130	1168	1500	1.83	6.56	0.76
	120	1405	1438	7.12(-4)	1.72(-3)	1.35
200	180	1330	1661	1.28(-3)	1.79(-4)	0.31
	150	1278	1600	1.55	2.92	0.29
	130	1209	1515	1.54	5.76	0.52
	120	1362	1422	8.72(-4)	1.71(-3)	1.45

TABLE 3

Four Layer Model Fits to A_{min}

$v_p(\frac{km}{sec})$	θ(deg)	R_1(km)	R_2(km)	R_3(km)	$\sigma_1(\frac{mhos}{m})$	$\sigma_2(\frac{mhos}{m})$	$\sigma_3(\frac{mhos}{m})$	ϵ^2
400	180	1290	1465	1479	1.58(-3)	2.76(-5)	2.42(-3)	0.29
	150	1198	1513	1520	2.17	5.66(-4)	4.06(-4)	0.48
	130	1280	1487	1519	1.08	6.46	3.61	1.00
	120	1286	1488	1496	9.34(-4)	7.75	8.12(-5)	1.70
300	180	1244	1457	1548	1.73(-3)	3.59	4.82(-4)	0.31
	150	1281	1440	1508	1.63	1.16	1.05(-3)	0.35
	130	1256	1499	1540	1.16	6.14	1.12(-4)	0.88
200	180	1263	1456	1713	1.56	4.45	1.09	0.29
	150	1277	1449	1600	1.56	2.91	2.89	0.29
	130	1249	1442	1483	1.76	2.62	1.50(-3)	0.37

TABLE 4

Core Plus Current Layer Model Fits to A_{min}

v_p ($\frac{km}{sec}$)	θ (deg)	R_1 (km)	R_2 (km)	σ_1 ($\frac{mhos}{m}$)	$\sigma\delta$ (mhos)	ϵ^2
400	180	1254	1467	1.91(-3)	84.0	0.39
	150	1236	1459	2.13	91.9	0.44
	130	1207	1440	2.38	109.7	0.64
	120	1170	1418	2.58	134.8	0.98
300	180	1282	1491	1.71	68.1	0.30
	150	1260	1476	1.91	78.5	0.34
	130	1212	1443	2.32	106.5	0.59
	120	1185	1408	2.11	141.6	1.12
200	180	1364	1587	1.20	31.8	0.32
	150	1329	1537	1.40	46.4	0.29
	130	1241	1457	2.03	92.6	0.42
	120	1155	1388	2.08	170.8	1.22

TABLE 5

Double Current Layer Fits to A_{min}

$v_p(\frac{km}{sec})$	θ (deg)	R_1 (km)	R_2 (km)	$\sigma_1\delta_1$ (mhos)	$\sigma_2\delta_2$ (mhos)	ϵ^2
400	180	1154	1463	505.1	93.3	0.31
	150	1147	1457	512.1	98.6	0.36
	130	1129	1440	528.1	113.5	0.55
	120	1108	1419	531.4	134.5	0.90
300	180	1176	1485	470.7	78.7	0.24
	150	1165	1473	485.8	86.6	0.27
	130	1132	1443	527.7	111.1	0.50
	120	1108	1409	455.4	144.6	1.07
200	180	1237	1559	380.0	45.1	0.39
	150	1209	1522	423.9	59.5	0.28
	130	1147	1454	509.8	100.7	0.34
	120	1100	1389	443.2	171.2	1.18

TABLE 6

Two Layer and Current Layer Model Fits to A_y

v_p ($\frac{km}{sec}$)	θ (deg)	R (km)	σ ($\frac{mhos}{m}$)	ϵ^2	R (km)	$\sigma\delta$ (mhos)	ϵ^2
400	180	1593	4.3(-4)	1.40	1509	109	3.29
	150	1586	4.5	1.51	1505	112	3.21
	130	1568	5.2	1.92	1493	121	3.10
	120	1547	6.2	2.53	1478	133	3.16
300	180	1613	3.8	1.24	1523	101	3.69
	150	1602	4.1	1.31	1515	106	3.43
	130	1572	5.1	1.79	1495	119	3.09
	120	1537	6.7	2.73	1470	139	3.17
200	180	1668	2.7	1.85	1560	84	6.00
	150	1644	3.1	1.45	1545	91	4.76
	130	1586	4.6	1.38	1504	114	3.13
	120	1520	7.6	2.72	1456	152	2.94

TABLE 7

Three Layer Model Fits to A_y

$v_p(\frac{km}{sec})$	θ(deg)	R_1(km)	R_2(km)	$\sigma_1(\frac{mhos}{m})$	$\sigma_2(\frac{mhos}{m})$	ϵ^2
400	180	1198	1594	2.1(-3)	4.4(-4)	0.95
	150	1185	1587	2.3	4.7	1.12
	130	1141	1568	2.9	5.4	1.64
	120	1127	1547	3.0	6.4	2.34
300	180	1199	1615	2.1	3.8	0.62
	150	1181	1603	2.4	4.2	0.78
	130	1156	1572	2.7	5.2	1.48
	120	1123	1538	2.7	6.8	2.59
200	180	1297	1681	1.3	2.4	0.52
	150	1244	1648	1.7	3.1	0.50
	130	1189	1587	2.2	4.7	1.00
	120	1289	1520	0.8	7.7	2.72

TABLE 8

Four Layer Model Fits to A_y

$v_p(\frac{km}{sec})$	θ(deg)	R_1(km)	R_2(km)	R_3(km)	$\sigma_1(\frac{mhos}{m})$	$\sigma_2(\frac{mhos}{m})$	$\sigma_3(\frac{mhos}{m})$	ϵ^2
300	180	1253	1389	1605	1.9(-3)	0.13(-4)	4.5(-4)	0.55
	150	1267	1465	1579	1.8	0.26	6.9	0.74
200	180	1240	1433	1694	1.6	4.3	2.1	0.50
	150	1231	1414	1650	1.8	3.6	3.0	0.51

TABLE 9

Core Plus Current Layer Model Fits to A_y

v_p ($\frac{km}{sec}$)	θ (deg)	R_1 (km)	R_2 (km)	σ_1 ($\frac{mhos}{m}$)	$\sigma\delta$ (mhos)	ε^2
400	180	1235	1523	2.2(-3)	87	0.71
	150	1230	1518	2.3	90	0.79
	130	1205	1504	2.6	101	1.09
	120	1180	1487	2.7	114	1.59
300	180	1270	1541	1.8	75	0.54
	150	1246	1531	2.1	83	0.61
	130	1211	1507	2.5	98	1.00
	120	1169	1479	3.0	121	1.78
200	180	1371	1607	1.1	45	0.55
	150	1326	1575	1.4	58	0.49
	130	1232	1517	2.2	90	0.72
	120	1153	1464	3.0	133	1.82

TABLE 10

Double Current Layer Model Fits to A_y

$v_p(\frac{km}{sec})$	θ(deg)	R_1(km)	R_2(km)	$(\sigma\delta)_1$(mhos)	$(\sigma\delta)_2$(mhos)	ϵ^2
400	180	1149	1521	529	92	0.63
	150	1141	1516	546	95	0.71
300	180	1171	1538	487	82	0.48
	150	1158	1529	512	87	0.54
200	180	1241	1593	355	55	0.67
	150	1210	1567	410	66	0.51
	130	1145	1516	532	95	0.64

FIGURE CAPTIONS

Fig. 1 Experimental transfer function amplitudes for the frequency interval $5 \times 10^{-4} < f < 4 \times 10^{-2}$ Hz. Coordinates x, y, and z are upward, eastward, and northward, respectively, at the Apollo 12 site. The lower frequency bound is determined by the time series swath of maximum length and the upper limit by the Nyquist frequency F_N of the Explorer 35 magnetometer and by noise considerations discussed in the text. The solid points are from one and two hour swaths and the open points from ten hour swaths of combined Explorer 35 and Lunar Surface Magnetometer (LSM) data. The error bars are the one standard deviation limits of the means. Error bars shown are representative of error bars for neighboring frequencies. Both A_y and A_z show the characteristic increase in response with frequency up to $f = 2 \times 10^{-2}$ Hz beyond which a rollover begins which can be ascribed to order higher than dipole in interaction of the solar wind with the Moon. A_x generally is about unity with a slight departure over the curve and a small rolloff at higher frequency. These data come from a much wider data base than those reported by SONETT et al. (1971a, b).

Fig. 2 The power spectral densities of Explorer 35 and LSM shown as a function of the "compass" heading angle, α , on the lunar surface. A_y corresponds to $\alpha = 0°$ while A_z corresponds to $\alpha = 90°$. Both show quasi-sinusoidal variations but the angles for the minima do not coincide. The data shown are for the frequency f = 0.005 Hz. The lighter traces labelled a and b correspond to the transfer functions determined from the power spectral densities according to the two algorithms given in the text. The variation of P_{EX} and P_{LSM} with angle is indicative of elliptically polarized radiation.

Fig. 3 Transfer function (A_y and A_{min}) amplitudes vs. frequency together with the direction α_{min} corresponding to the minimum value of A_y . The effect of rotation is most pronounced at the higher frequencies where the higher order multipoles supplement the dipole interaction. The plateau in α_{min} is consistent with a noise source attributable to the interaction of the dynamic pressure fluctuations of the solar wind with the permanent field at the Apollo 12 site. The low frequency behavior of α_{min} is unexplained at the present time.

Fig. 4 Illustrative calculation of the high frequency transfer function behavior vs. angle α for 4 frequencies. The hypothesized Explorer power (incident wave), the LSM response power (incident + scattered wave), and the transfer function are shown for the different frequencies. The calculation is carried out for a single current layer Moon with $\theta = 130°$ and $v_p = 200$ km/sec. The current layer is at R = 1500 km with a $\sigma\delta$ value of 150 mhos. The increase in angle of minimum response with frequency is similar to the increase seen in the data.

Fig. 5 Histograms of α_{min} at f = 0.04 Hz and 0.01 Hz showing the statistical favoring of the direction perpendicular to the permanent field, B_p , in the lower frequency data and a bimodal modification at the upper frequency limit. The latter shows the peak perpendicular to B_p , i.e. $\alpha_{min} = 27°$, and an additional peak suggesting a two component source of noise. The wide low level background, i.e. the distribution of values of α_{min} , is indicative of possible other additional components which contribute to the noise vector.

Fig. 6 Geometry of the generalized induction problem. A plane wave with wave vector $\underline{k}$ is shown incident upon the Moon. In general the solar wind bulk velocity vector, $\underline{v}_s$, will not be colinear with $\underline{k}$. A_θ and A_φ are the transfer functions at the site of LSM resolved into a spherical polar system whose polar angle is given by θ and azimuth by φ . Generally $A_\theta \geq A_\varphi$.

Fig. 7 Theoretical behavior of idealized transfer functions showing the effect of varying θ and v_p . These effects are most pronounced at the higher frequencies where the geometry dependence becomes important. The calculations are carried out for the three layer (3L) Moon conductivity model discussed in the text. The importance of the assigned values of θ and v_p are amply demonstrated. The wavelength varies with v_p modifying the response in the intermediate scattering regime where most of the lunar response lies.

Fig. 8 Bulk conductivity models of the Moon for two layer (2L), three layer (3L), four layer (4L), current layer (CL), double current layer (DCL), and core

Fig. 8 (continued)

plus current layer (CCL) models. All models here are iterative best fits to A_{min} data using v_p = 200 km/sec and $\theta = 150^\circ$. These models are not the best fits when other values of v_p and θ are permitted; for those models the reader is referred to the tabulations. The hyperbolae define current layers for which $\sigma\delta$ = constant, approximating the effect of the very thin layers used in the current layer calculations.

Fig. 9 Forward calculation of the transfer function amplitude corresponding to the conductivity models shown in Fig. 8. The 3L, 4L, and CCL models all yield transfer functions having values too close to plot separately on this scale. The experimental A_{min} values are shown for reference. The legend lists the values of ϵ^2 belonging to each model fitted. The experimental value of ϵ^2 (the sum of the squares of the standard deviations of the means) for A_{min} is 0.65; thus all models shown here are reasonable fits with the exception of the 2L and CL cases.

Fig. 10 Comparison of the experimental (A_{min}) transfer function amplitude and the transfer function

Fig. 10 (continued)

amplitudes corresponding to three layer (3L) models using a variable value of θ . Each model is an iterative best fit under the conditions v_p = 200 km/sec and θ the value associated with the model. All models are shown in the insert for reference. The fit $\theta = 120^\circ$ fit yields a "spike" in the conductivity.

Fig. 11 Models and transfer function amplitudes similar to those of Fig. 10 but with v_p as variable and θ fixed at 150°.

Fig. 12 Comparison of the 3L best fits to A_y and A_{min} with two versions of the DYAL and PARKIN (1971a,b; private communication) models based upon the transient response measured on the dark side of the Moon. These latter correspond to three layer lunar models: for DP_1 the shell (between the core and crust) conductivity is 10^{-4} mhos/m and the radius is 0.95 Rm for DP_2 the conductivity of the shell is 3×10^{-4} mhos/m and the radius is 0.95 Rm. Both models have a core of conductivity 10^{-2} mhos/m and a radius of 1044 km. All fits are for v_p = 200 km/sec and $\theta = 150^\circ$. Rm is the lunar radius.

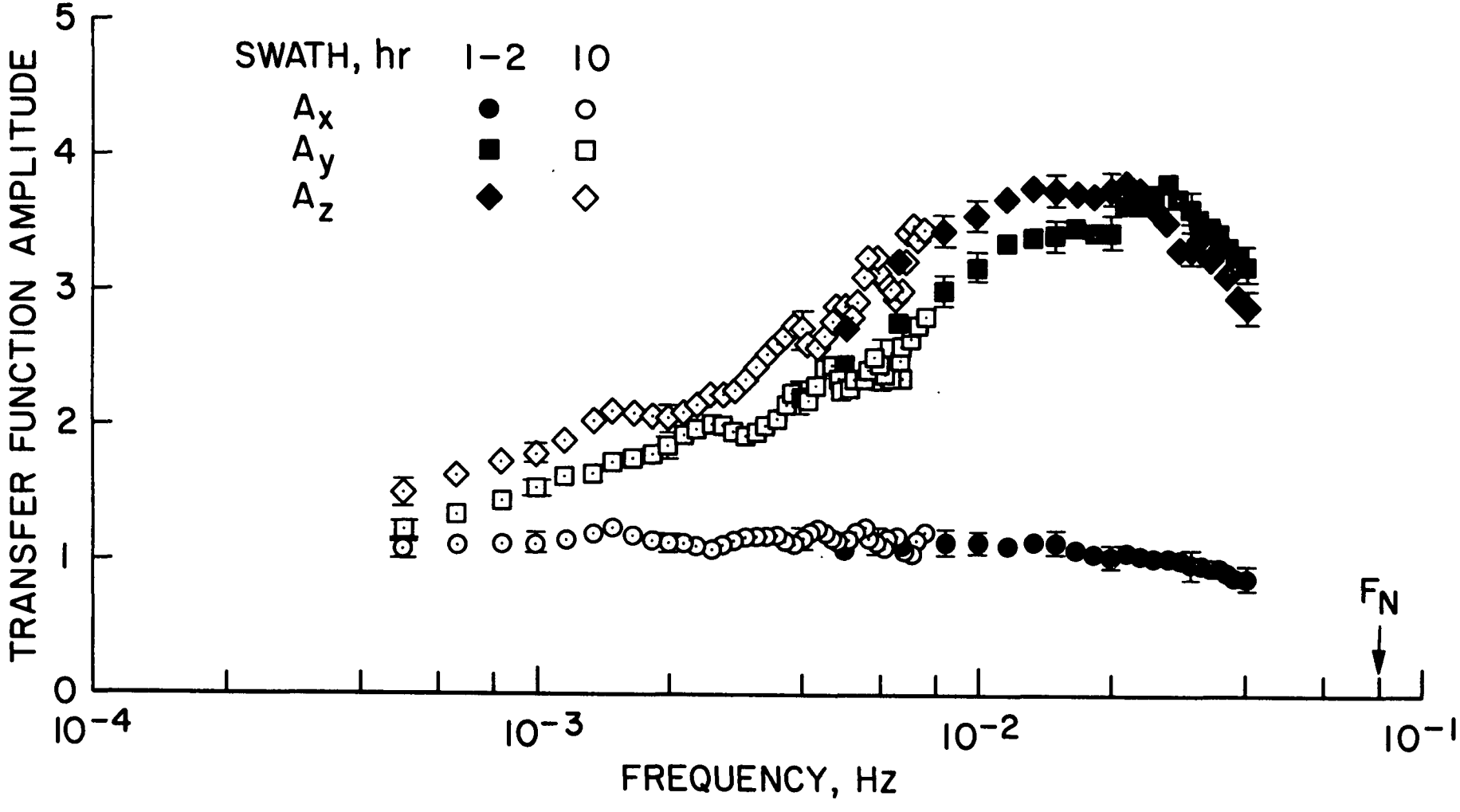
SWATH, hr
1-2
10
A_x
A_y
A_z
TRANSFER FUNCTION AMPLITUDE
0
1
2
3
4
5
10^{-4}
10^{-3}
10^{-2}
10^{-1}
F_N
FREQUENCY, Hz

Fig. 1

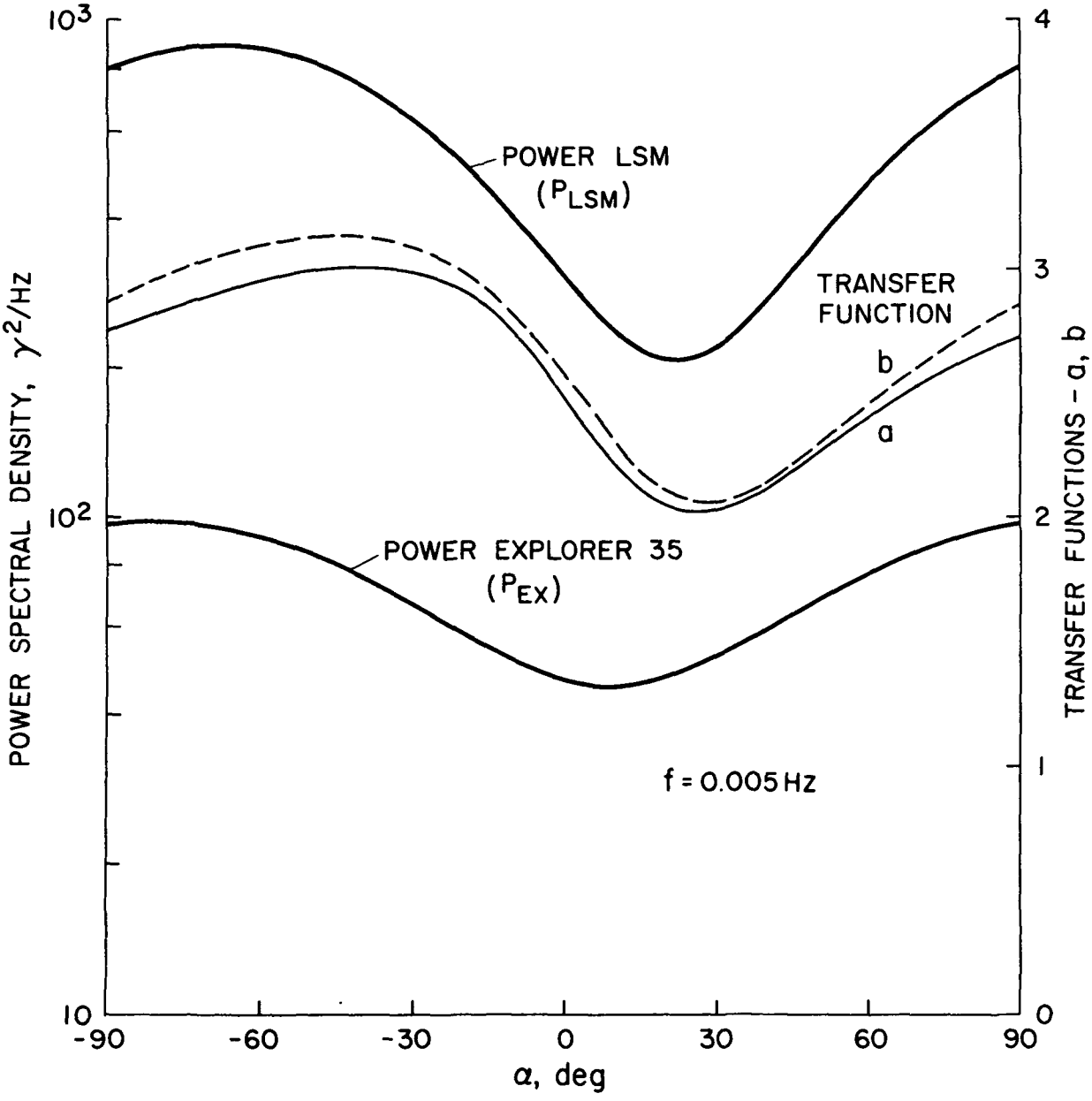

Fig. 2

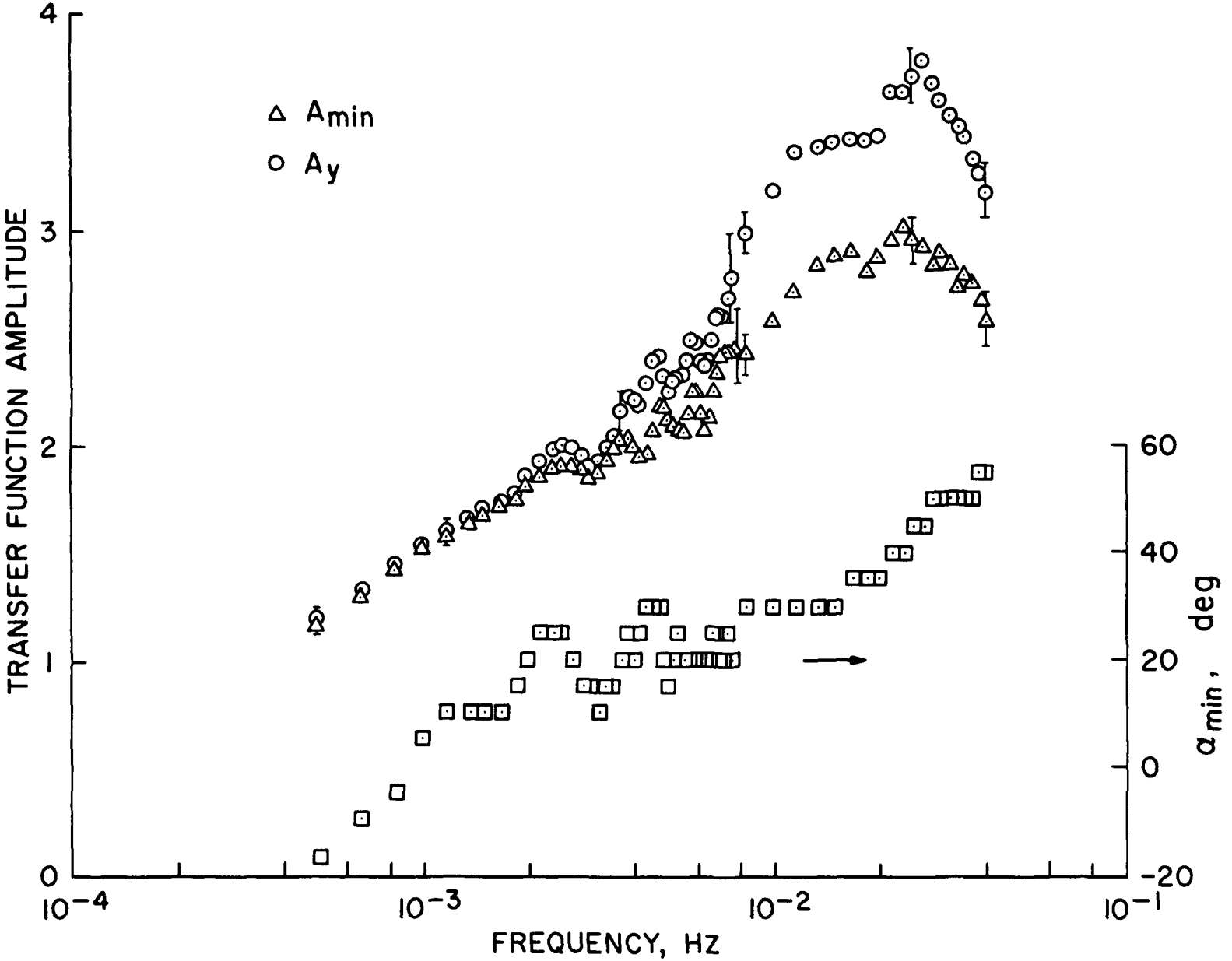

Fig. 3

NATIONAL AERONAUTICS AND SPACE ADMINISTRATION
AMES RESEARCH CENTER, MOFFETT FIELD, CALIFORNIA

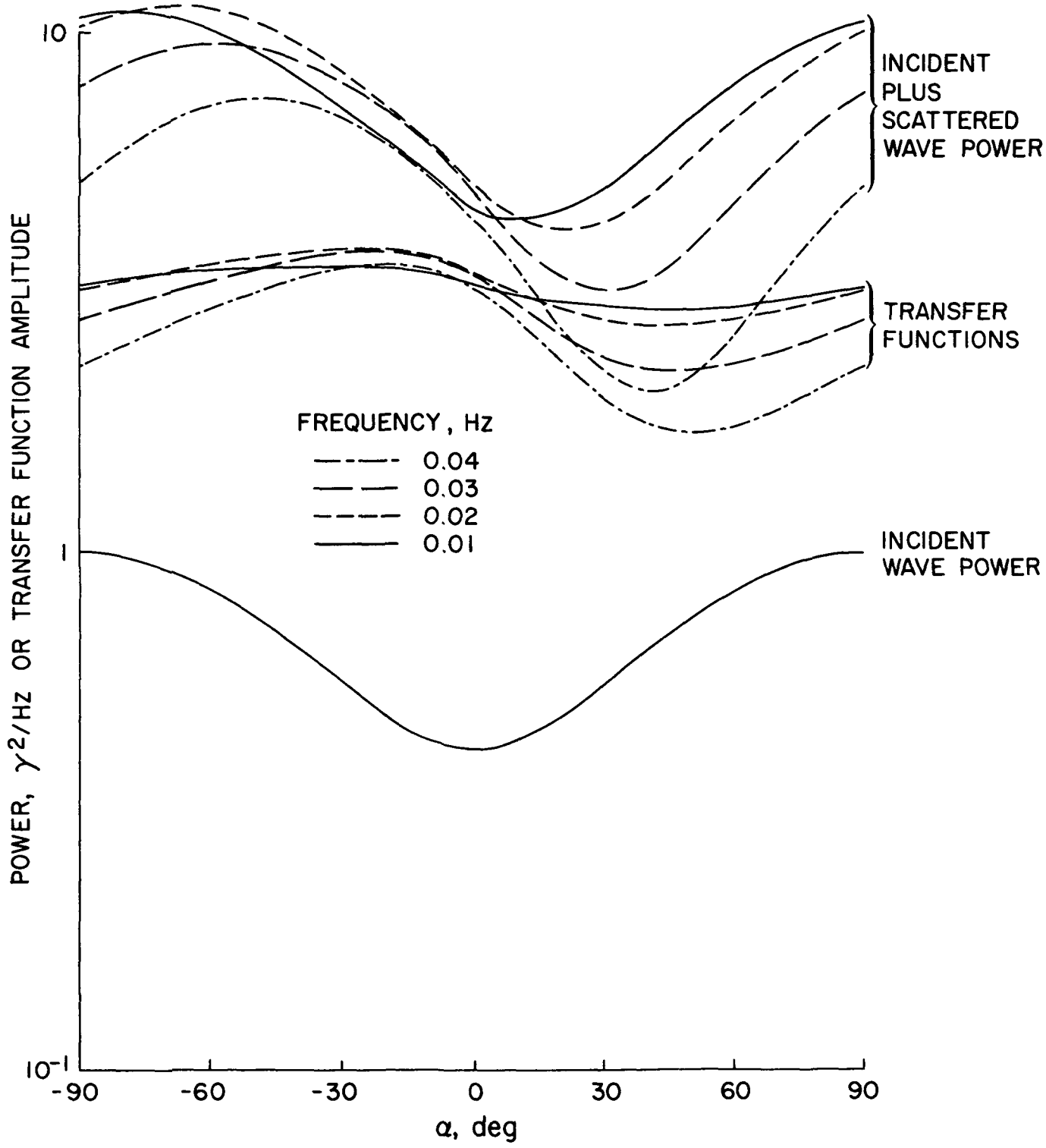
10
1
10^{-1}
POWER, γ^2/Hz OR TRANSFER FUNCTION AMPLITUDE
INCIDENT
PLUS
SCATTERED
WAVE POWER
TRANSFER
FUNCTIONS
FREQUENCY, Hz
0.04
0.03
0.02
0.01
INCIDENT
WAVE POWER
-90
-60
-30
0
30
60
90
α, deg

Fig. 4

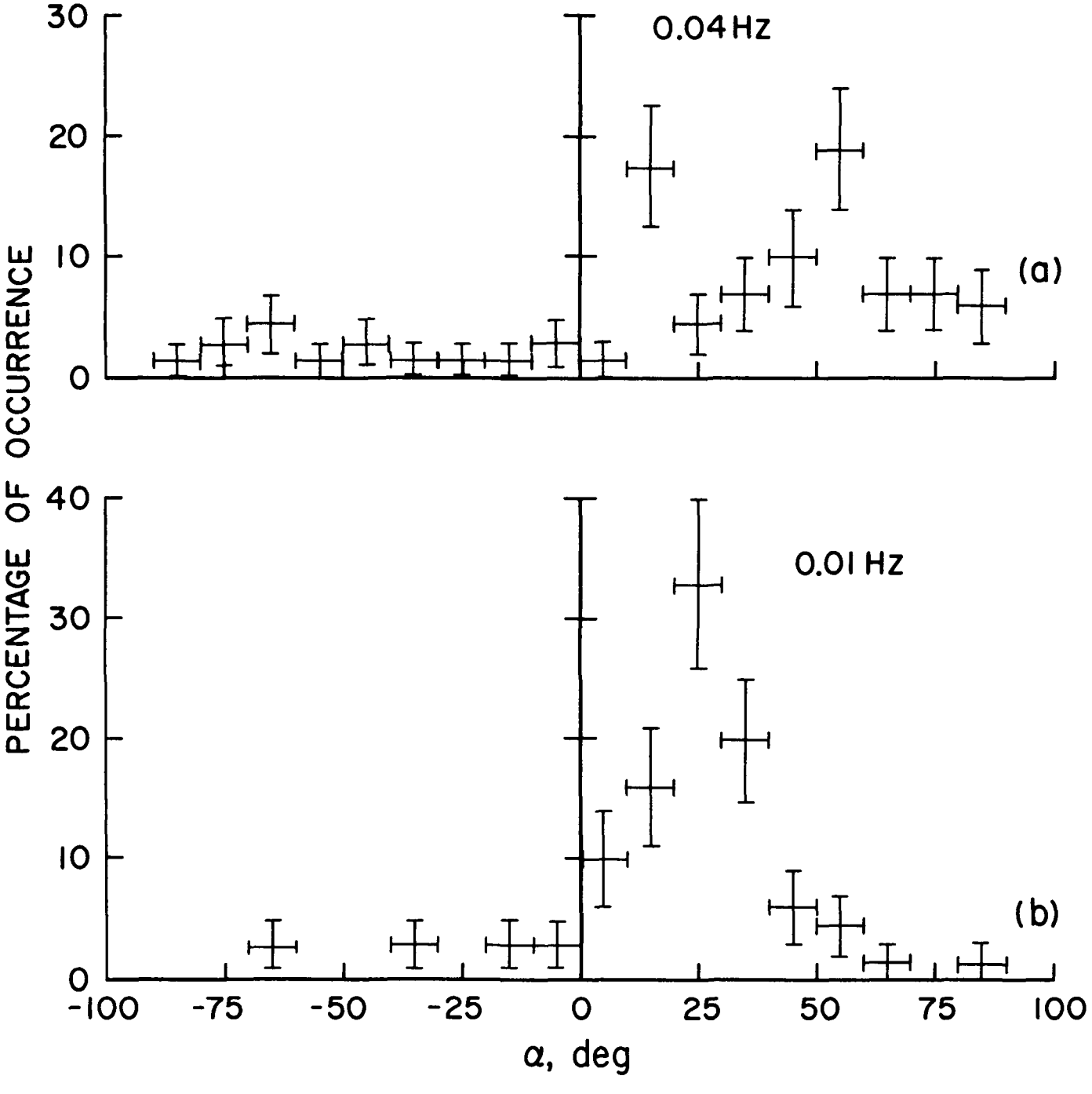
0.04 Hz
(a)
0.01 Hz
(b)
PERCENTAGE OF OCCURRENCE
α, deg
30
20
10
0
40
30
20
10
0
-100
-75
-50
-25
0
25
50
75
100

Fig. 5

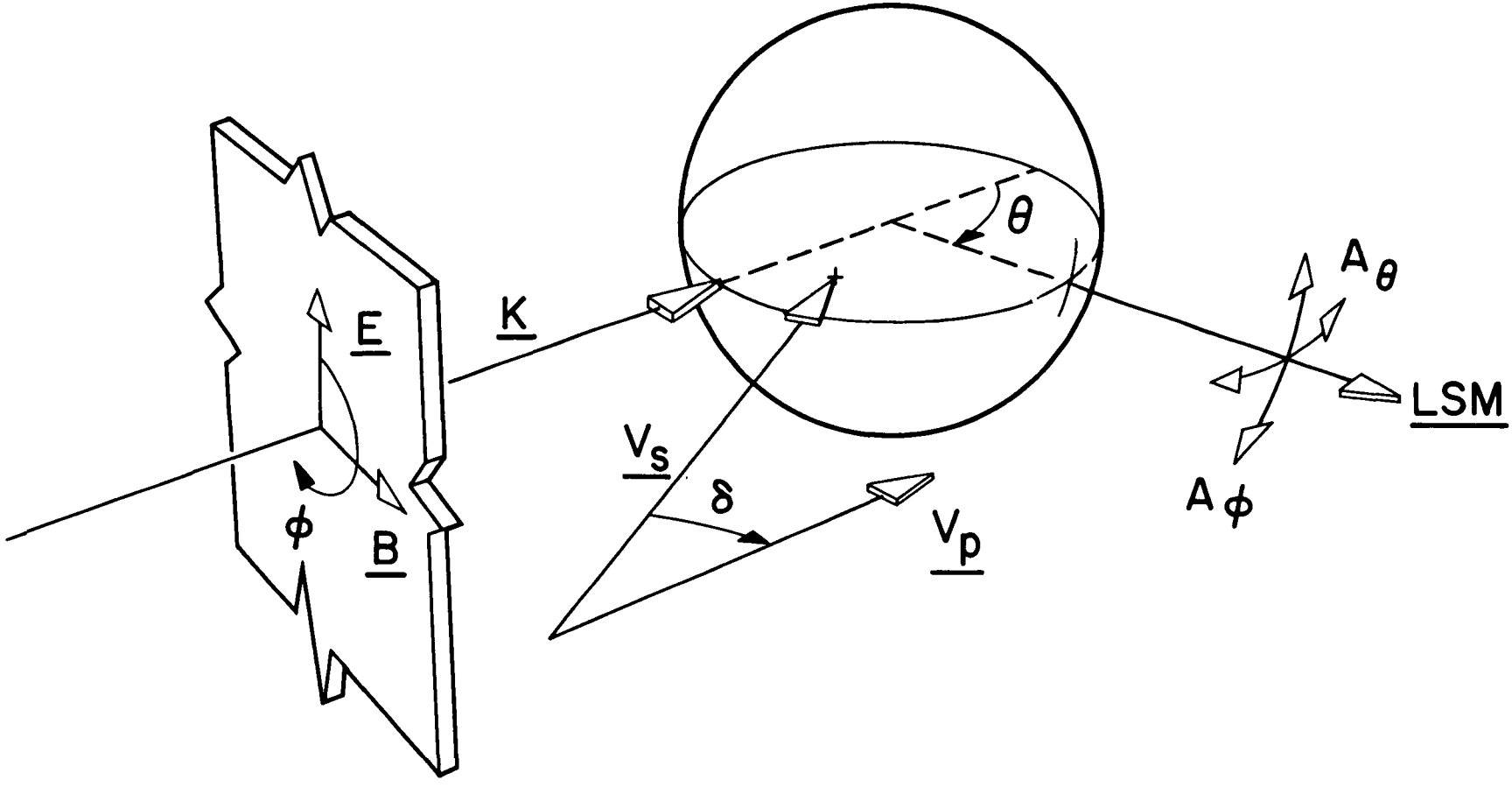

Fig. 6

NATIONAL AERONAUTICS AND SPACE ADMINISTRATION
AMES RESEARCH CENTER, MOFFETT FIELD, CALIFORNIA

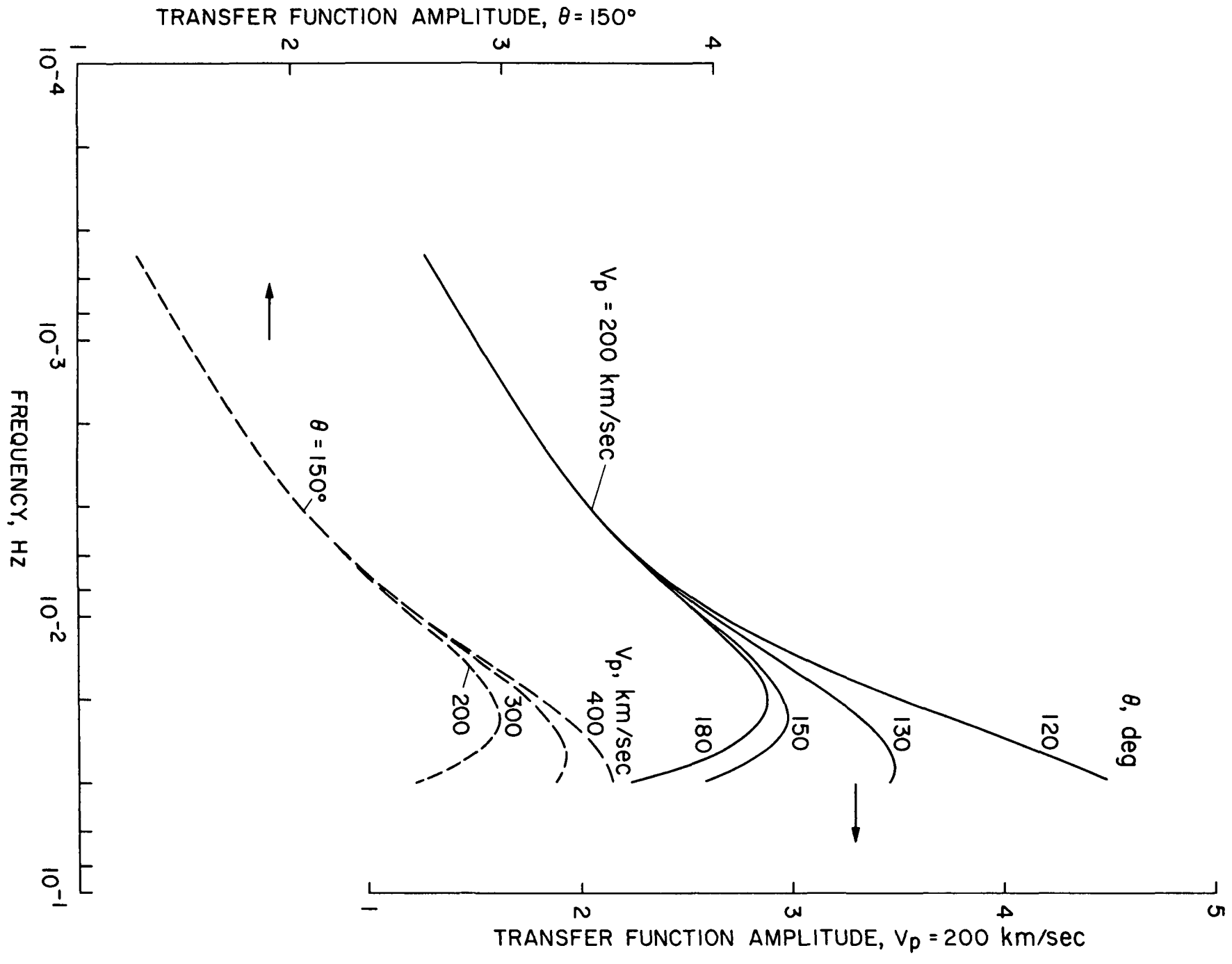
TRANSFER FUNCTION AMPLITUDE, θ = 150°
FREQUENCY, HZ
10⁻⁴
10⁻³
10⁻²
10⁻¹
1
2
3
4
θ = 150°
Vp = 200 km/sec
Vp, km/sec
200
300
400
θ, deg
180
150
130
120
TRANSFER FUNCTION AMPLITUDE, Vp = 200 km/sec
5

Fig. 7

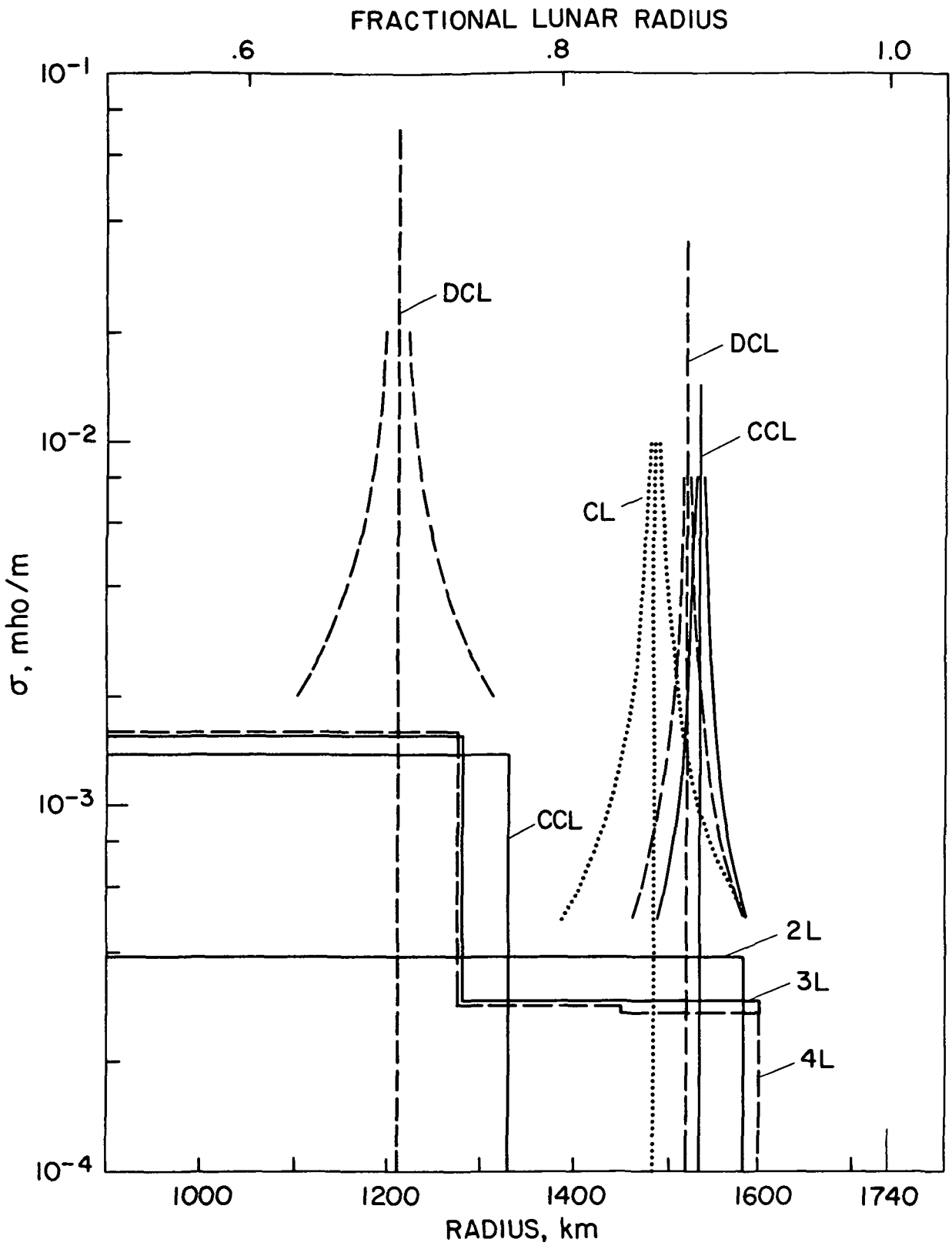

Fig. 8

NATIONAL AERONAUTICS AND SPACE ADMINISTRATION
AMES RESEARCH CENTER, MOFFETT FIELD, CALIFORNIA

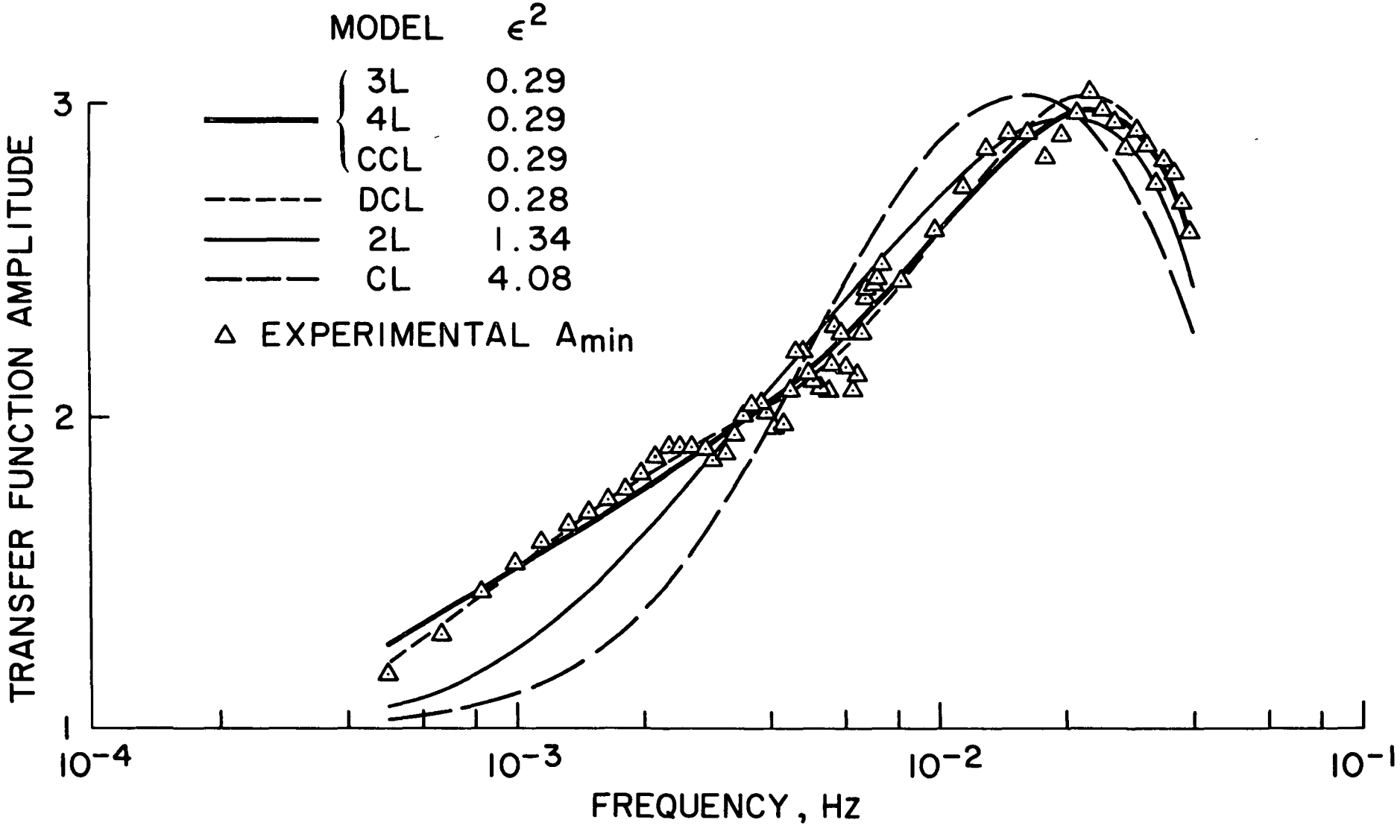
MODEL
ϵ^2
3L 0.29
4L 0.29
CCL 0.29
DCL 0.28
2L 1.34
CL 4.08
△ EXPERIMENTAL A_{min}
TRANSFER FUNCTION AMPLITUDE
3
2
1
10^{-4}
10^{-3}
10^{-2}
10^{-1}
FREQUENCY, Hz

Fig. 9

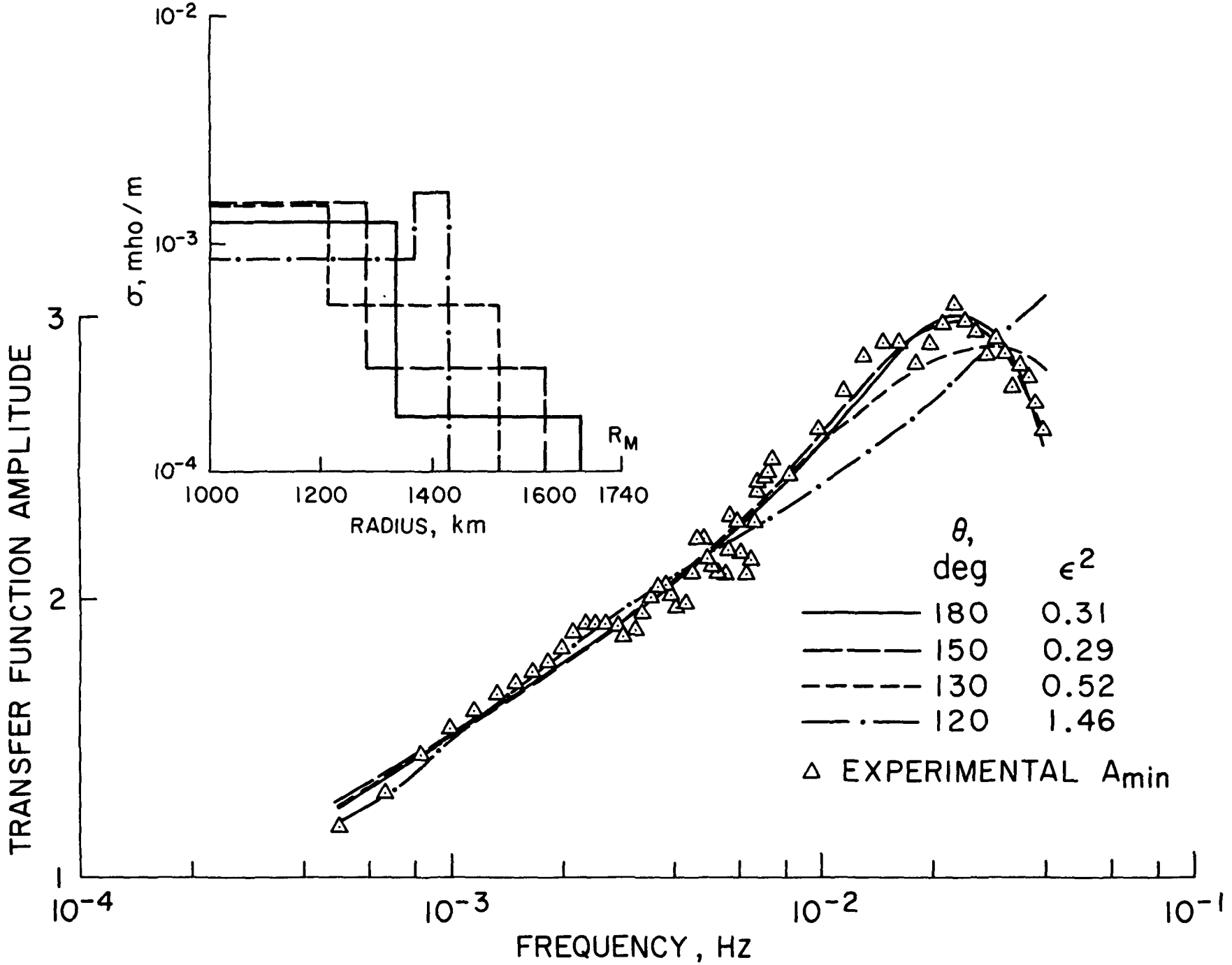
TRANSFER FUNCTION AMPLITUDE
FREQUENCY, HZ
σ, mho/m
RADIUS, km
R_M
θ, deg
ε²
180 0.31
150 0.29
130 0.52
120 1.46
△ EXPERIMENTAL Amin

Fig. 10

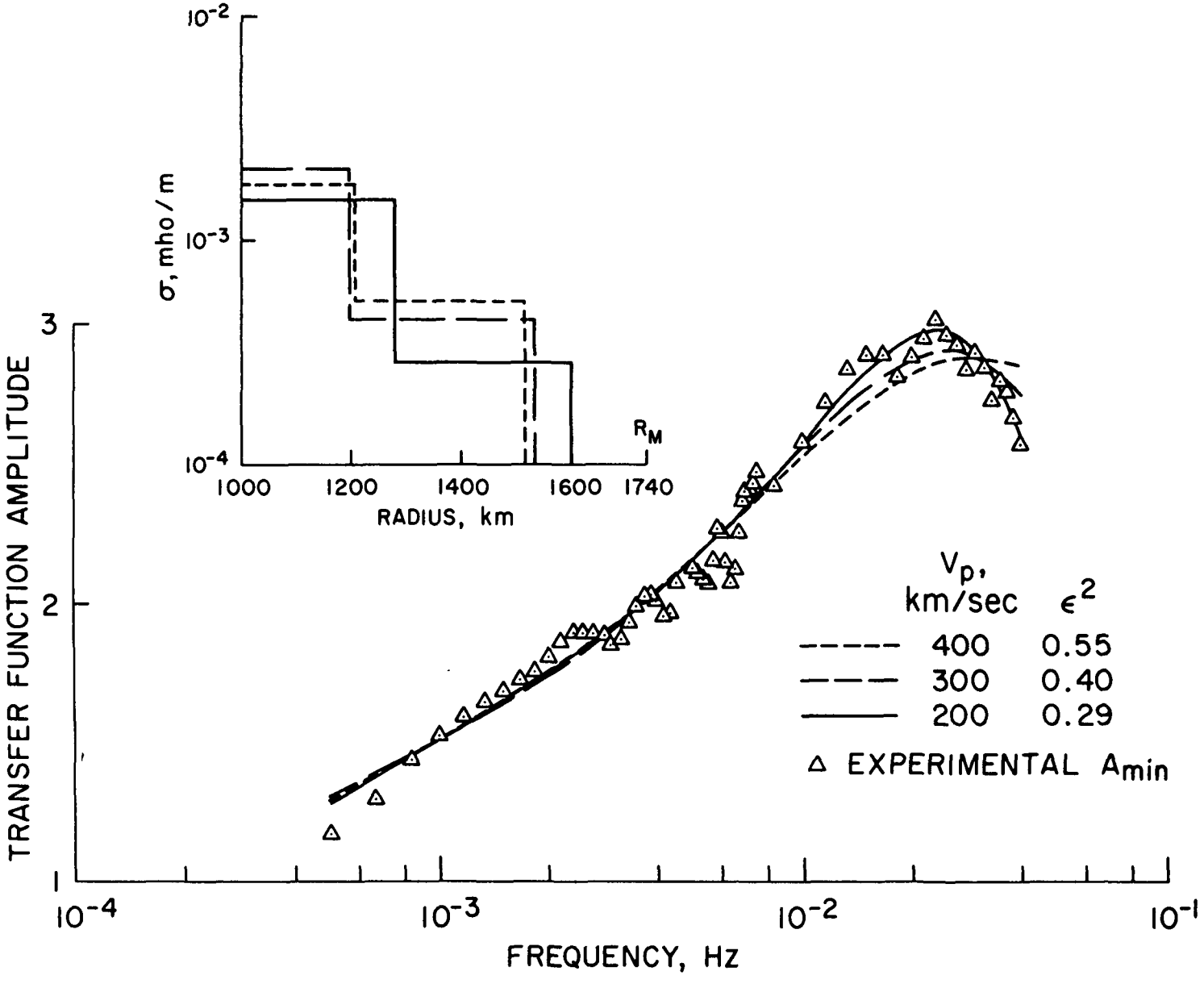

Fig. 11

NATIONAL AERONAUTICS AND SPACE ADMINISTRATION
AMES RESEARCH CENTER, MOFFETT FIELD, CALIFORNIA

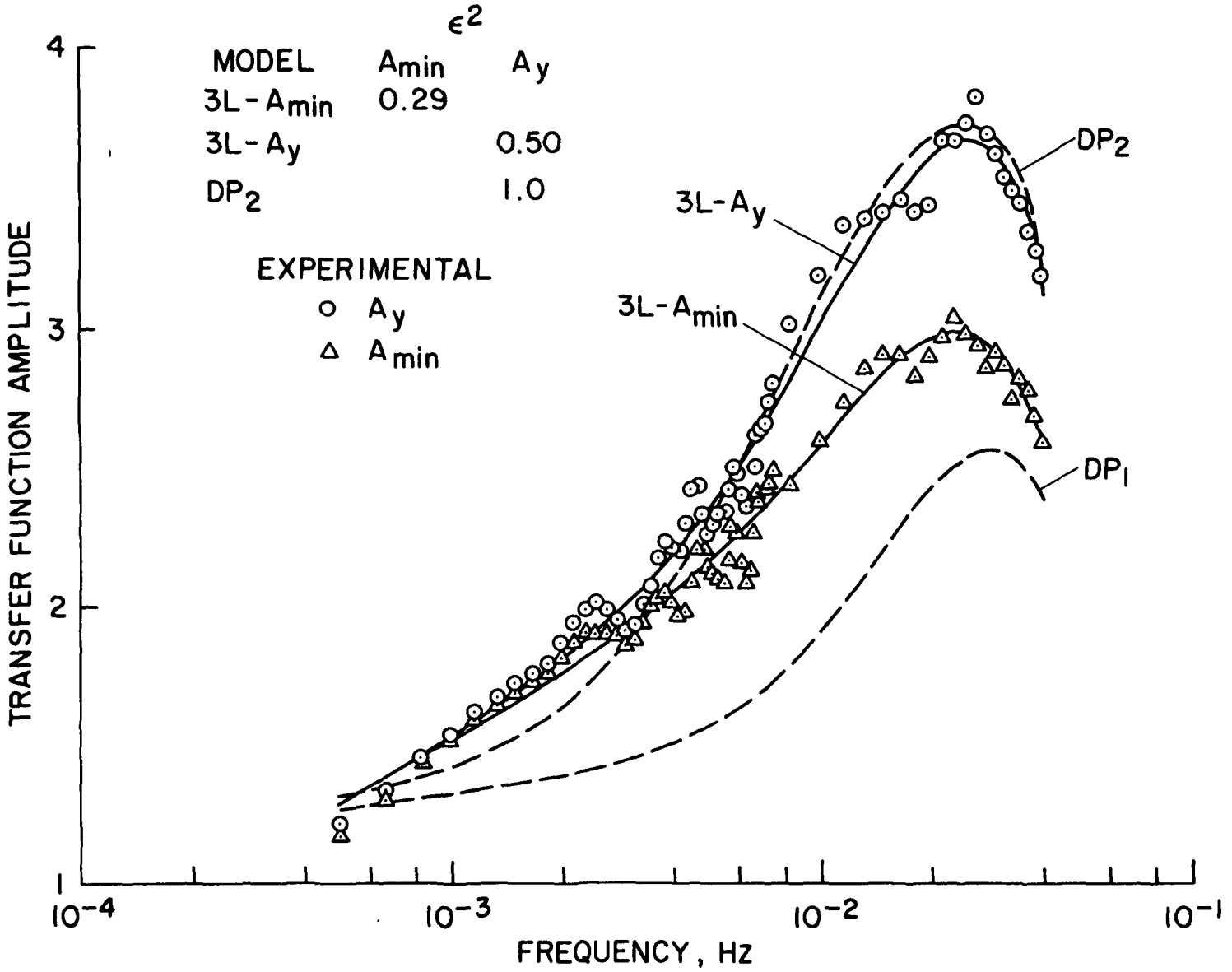
ϵ^2
MODEL
A_{min}
A_y
3L-A_{min} 0.29
3L-A_y 0.50
DP_2 1.0
EXPERIMENTAL
A_y
A_{min}
DP_2
3L-A_y
3L-A_{min}
DP_1
TRANSFER FUNCTION AMPLITUDE
FREQUENCY, HZ
4
3
2
1
10^{-4}
10^{-3}
10^{-2}
10^{-1}

Fig. 12